TITLE

Phenotypic complexities of rare heterozygous neurexin-1 deletions

AUTHORS

Michael B. Fernando[1,2,4,8], Yu Fan[3*], Yanchun Zhang[3*], Alex Tokolyi[5], Aleta N. Murphy[1,2,4], Sarah Kammourh[3], P.J. Michael Deans[8], Sadaf Ghorbani[7,8], Ryan Onatzevitch[2], Adriana Pero[3], Christopher Padilla[3], Sarah Williams[1,2,4], Erin K. Flaherty[1,2,4], Iya A. Prytkova[1,2,4], Lei Cao[3] , David A. Knowles[5,6,], Gang Fang[3#], Paul A. Slesinger,[1,2#] & Kristen J. Brennand[2-4,8#]

AFFILIATIONS

[1]Graduate School of Biomedical Science, Icahn School of Medicine at Mount Sinai, New York, NY 10029

[2]Nash Family Department of Neuroscience, Icahn School of Medicine at Mount Sinai, New York, NY 10029

[3]Department of Genetics and Genomics, Icahn School of Medicine at Mount Sinai, New York, NY 10029

[4]Friedman Brain Institute, Black Family Stem Cell Institute, Pamela Sklar Division of Psychiatric Genomics, Icahn School of Medicine at Mount Sinai, New York, NY 10029

[5]New York Genome Center, New York, NY, 10013

[6]Departments of Computer Science, Systems Biology, and Data Science Institute, Columbia University, New York, NY, USA, 10027

[7]Haukeland University Hospital, Bergen, Norway

[8]Department of Psychiatry, Yale School of Medicine, New Haven, CT, 06520

*These authors contributed equally

[#]Correspondence: kristen.brennand@yale.edu, paul.slesinger@mssm.edu and gang.fang@mssm.edu

KEYWORDS

Human induced pluripotent stem cells; *NRXN1*; alternative splicing; glutamatergic neurons; GABAergic neurons; genomics; neuropsychiatric disorder; disease modeling; precision medicine

ABSTRACT

Given the large number of genes significantly associated with risk for neuropsychiatric disorders, a critical unanswered question is the extent to which diverse mutations --sometimes impacting the same gene-- will require tailored therapeutic strategies. Here we consider this in the context of rare neuropsychiatric disorder-associated copy number variants (2p16.3) resulting in heterozygous deletions in *NRXN1*, a pre-synaptic cell adhesion protein that serves as a critical synaptic organizer in the brain. Complex patterns of *NRXN1* alternative splicing are fundamental to establishing diverse neurocircuitry, vary between the cell types of the brain, and are differentially impacted by unique (non-recurrent) deletions. We contrast the cell-type-specific impact of patient-specific mutations in *NRXN1* using human induced pluripotent stem cells, finding that perturbations in *NRXN1* splicing result in divergent cell-type-specific synaptic outcomes. Via distinct loss-of-function (LOF) and gain-of-function (GOF) mechanisms, *NRXN1*$^{+/-}$ deletions cause decreased synaptic activity in glutamatergic neurons, yet increased synaptic activity in GABAergic neurons. Reciprocal isogenic manipulations causally demonstrate that aberrant splicing drives these changes in synaptic activity. For *NRXN1* deletions, and perhaps more broadly, precision medicine will require stratifying patients based on whether their gene mutations act through LOF or GOF mechanisms, in order to achieve individualized restoration of *NRXN1* isoform repertoires by increasing wildtype, or ablating mutant isoforms. Given the increasing number of mutations predicted to engender both LOF and GOF mechanisms in brain disorders, our findings add nuance to future considerations of precision medicine.

48 **MAIN**

49 Neurexins are pre-synaptic cell adhesion proteins that act as synaptic organizers[1]. There are
50 three neurexin genes (*NRXN1*, *NRXN2*, and *NRXN3*) in mammals and each is highly alternatively
51 spliced to produce hundreds of isoforms, primarily categorized into long alpha and shorter beta
52 isoforms[2]. The complex alternative splicing of neurexins expands protein-protein interaction
53 capabilities[3], allowing neurexins to interact with diverse post-synaptic ligands to establish and
54 maintain neurotransmission. *NRXN1*α splice variants are specific to brain regions[4] and between
55 cell types[5], but the cell-type-specific functional impact of individual isoforms remains unclear.
56 Although rare in the population, large copy number variations (deletions or duplications) at the
57 *NRXN1* locus 2p16.3, particularly those deleting exonic regions, are highly penetrant, pleiotropic,
58 and are strongly associated with several neuropsychiatric diseases, including schizophrenia
59 (odds ratio 14.4[6]), autism spectrum disorder (odds ratio 14.9[7]), epilepsy (odds ratio 9.91[8]),
60 intellectual disability (odds ratio 7.47[9]) and Tourette's syndrome (odds ratio 20.3[10]). Deletions in
61 *NRXN1* are non-recurrent (that is, they vary in size and location), making it difficult to determine
62 the molecular mechanisms underlying their diverse clinical symptoms (e.g., diagnosis, severity,
63 prognosis, and age-of-onset). In rodent studies, gene knockouts (KO) of *NRXNs* are sufficient to
64 produce an array of excitatory and inhibitory synaptic phenotypes[1]. However, heterozygous
65 deletions yield only modest behavioral and physiological changes *in vivo*[11]. By contrast, *in vitro*
66 studies of engineered heterozygous *NRXN1*$^{+/-}$ human neurons reveal robust changes in excitatory
67 neurotransmission that are not recapitulated in matched *NRXN1*$^{+/-}$ mouse neurons[12,13], and
68 studies that utilize patient derived *NRXN1*$^{+/-}$ neurons have yet to deconvolute complex phenotypes
69 in a cell-type and genotype specific manner[12,14]. Altogether, neurexins possess unique human
70 neurobiology, and therefore, the impact of distinct patient-specific *NRXN1*$^{+/-}$ must be specifically
71 evaluated in human models with an important consideration of how unique *NRXN1*$^{+/-}$ deletions
72 impact splicing patterns and neuronal function across distinct cell-types.

73 Human induced pluripotent stem cell (hiPSC)-derived neurons provide an ideal platform to study
74 *NRXN1α* alternative splicing. Previously we established that hiPSC-derived forebrain cultures,
75 comprised of a mixture of glutamatergic and GABAergic neurons with astroglia, recapitulate the
76 diversity of *NRXN1α* alternative splicing observed in the human brain, cataloguing 123 high-
77 confidence *NRXN1α* isoforms[15]. Furthermore, using patient-derived *NRXN1*$^{+/-}$ hiPSCs with unique
78 5'- or 3'-deletions in the gene, we uncovered wide-scale reduction in wildtype *NRXN1α* isoform
79 levels and, robust expression of dozens of novel isoforms from the 3'-deletion allele only[15].
80 Overexpression of individual wildtype isoforms (WT) ameliorated reduced neuronal activity in

81 patient-derived *NRXN1*$^{+/-}$ hiPSC-neurons in a genotype-dependent manner, whereas mutant
82 isoform (MT) expression decreased neuronal activity levels in control hiPSC-neurons[15]. We
83 therefore hypothesized that 5'-deletions of the promoter region represent classical loss-of-
84 function (LOF), while robust expression of novel 3'-specific MT isoforms confer a gain-of-function
85 (GOF) effect that cannot be rescued by overexpression of WT isoforms. Although *NRXN1* splicing
86 varies between the cell types of the brain, the impact of non-recurrent *NRXN1*$^{+/-}$ deletions on cell-
87 type-specific splicing patterns and synaptic function remains untested.

88 Neurexin signaling impacts both glutamatergic and GABAergic synapse properties[3,16], suggesting
89 that neurexins may regulate excitatory and inhibitory balance, which is strongly implicated across
90 neuropsychiatric disorders[17]. Given its multifaceted roles, the lack of mechanistic understanding
91 of how aberrant *NRXN1* splicing impacts neuronal physiology in a cell-type *and* genotype-
92 dependent manner presents a significant challenge for therapeutic targeting. To discover the
93 disease mechanisms that underpin *NRXN1*$^{+/-}$ deletions, we compared excitatory and inhibitory
94 neurons, across LOF and GOF deletions, to specifically evaluate cell-autonomous phenotypes
95 arising from distinct *NRXN1*$^{+/-}$ deletions. We identified points of phenotypic divergence across
96 glutamatergic and GABAergic neurons, which were independently validated in isogenic
97 experiments, thereby establishing causal relationships between aberrant splicing and synaptic
98 dysfunction. Finally, we evaluated novel therapeutic agents for *NRXN1*$^{+/-}$ deletions based on
99 LOF/GOF stratified patient mechanisms.

100 RESULTS

101 Patient-specific *NRXN1*$^{+/-}$ mutations produces differential *NRXN1* splicing patterns across
102 glutamatergic and GABAergic neurons

103 To examine the impact of *NRXN1*$^{+/-}$ deletions in two different neuronal cell types, we used
104 transcription-factor based lineage conversion of hiPSCs to generate excitatory glutamatergic
105 neurons or inhibitory GABAergic neurons from our previous cohort[14] (all available clinical and
106 experimental information reported in **Supplementary Table 1**). Two cases sharing a ~115-kb
107 deletion in the 5'-region of *NRXN1* (5'-Del), affecting the alpha-transcript promoter, represent the
108 LOF condition. Two additional cases sharing a ~136-kb deletion in the 3'-region of *NRXN1* (3'-
109 Del), impacting two alternative splice sites (SS4, SS5) across three exons (21-23), robustly
110 express unique MT isoforms from the affected allele and therefore represent the GOF condition[15].
111 For controls, we used passage-matched hiPSCs from four healthy sex-balanced subjects (**Fig.**

112 **1a,b**). Transient overexpression of *NGN2* in hiPSCs produced iGLUT neurons that were >95%
113 pure glutamatergic neurons, robustly expressed glutamatergic genes, released glutamate, and
114 produced spontaneous synaptic activity by day 21 in vitro[18,19]. On the other hand, transient
115 overexpression of *ASCL1* and *DLX2* yielded iGABA neurons that were >80% positive for
116 expressing GABA and GAD1/2 by day 35 in vitro, and possessed mature physiologic properties
117 of inhibitory neurons by day 42[20,21]. Immunostaining confirmed expression of neurotransmitter
118 transporters, vGLUT1 and vGAT for iGLUT and iGABA neurons, respectively (**Fig. 1c,h**). RNA-
119 sequencing (RNAseq) further validated iGLUT (DIV21) and iGABA (DIV35) neuronal induction in
120 all donors (**Fig. 1d,i**).

121 Despite cell-type-specific *NRXN1* isoform profiles reported in healthy brains[5] and neurons[15],
122 aberrant *NRXN1* alpha/beta exon expression patterns appeared similar between *NRXN1*$^{+/-}$ iGLUT
123 and iGABA neurons (**Fig. 1e,j**), whereby alpha exon expression (exons 2-18) decreased for 5'-
124 Del and increased for 3'-Del in both types of neurons (iGLUT 5'-Del $p = 0.0031$; 3'-Del, $p = 0.0086$,
125 1-way ANOVA, Dunnett's test; iGABA 5'-Del $p = 0.0004$; 3'-Del, $p < 0.0001$, 1-way ANOVA,
126 Dunnett's test). To investigate changes in alternative splicing, we applied LeafCutter[22], an
127 annotation free analysis to estimate differential splicing events visualized by splicegraphs
128 denoting change of percent-spliced-in (ΔPSI) ratios across the *NRXN1* gene at annotated splice
129 sites (SS1-6) and novel unannotated junctions (**Fig 1b**). Differential splicing analysis between
130 iGLUT and iGABA neurons produced a single significant cluster (out of nine identified), centered
131 around SS3 (**Extended Data Fig. 1a**, $p = 0.01960$, Bonferroni corrected), suggesting that the
132 majority of isoforms were conserved between the two cell-types, as previously reported[15].

133 Specifically, we detected both canonical and noncanonical splicing patterns in 5'-Del and 3'-Del
134 neurons, relative to controls. Splicing of *NRXN1* transcript was perturbed at two locations in 5'-
135 Del neurons. The first change in splicing occurred at the alternative transcription start site,
136 reducing splicing of beta-exon transcripts into alpha-exon transcripts (henceforth referred to as
137 $\beta \rightarrow \alpha$), as expected given the affected alpha promoter. We observed a significant reduction in 5'-
138 Del iGABA neurons (ΔPSI -0.187, $p = 0.0146$, Bonferroni corrected), and a more modest decrease
139 in iGLUT neurons (ΔPSI -0.086, $p = 0.1821$, Bonferroni corrected), consistent with a LOF. In 5'-
140 Del iGLUT neurons, we also detected differential splicing at SS4 inclusion (ΔPSI -0.046, $p =$
141 0.006, Bonferroni corrected) **(Fig. 1f,k)**. For 3'-Del neurons, we observed a robust increase in a
142 mutant splice junction between exon 20-24 in iGLUT (ΔPSI 0.227, $p = 1.09E-19$) and iGABA
143 (ΔPSI 0.23, $p = 6.93E-23$, Bonferroni corrected) neurons, concurrent with reduced wildtype
144 splicing around SS4 and SS5 **(Fig. 1g,l),** consistent with a GOF. Interestingly, STAR-family RNA-

145 binding proteins that regulate *NRXN1* splicing at SS4[23–26] were also dysregulated across cell-
146 types and genotypes **Extended Data Fig**. **1b,f**). Taken together, these differential splicing
147 patterns support our hypothesis that 5'-Del and 3'-Del mutations confer LOF/GOF phenotypes,
148 either by reducing $\beta \rightarrow \alpha$ splicing or producing novel MT isoforms, respectively.

149 ***NRXN1*$^{+/-}$ mutations broadly impact synaptic and neurodevelopmental pathways in induced**
150 **and organoid-derived glutamatergic and GABAergic neurons**

151 To unbiasedly evaluate the transcriptomic impact of *NRXN1*$^{+/-}$ deletions, and their unique splicing
152 patterns, we utilized differential expression analysis[27] in iGLUT and iGABA neurons, which
153 revealed overlap of FDR-corrected differentially expressed genes (DEGs) across cell
154 types/genotypes (e.g., *FAM66D, TTC34, GALNT9*), and represented gene sets related to synaptic
155 function (via SynapseGO[28]) (**Fig. 2a-d, j-m**). To test for pathway enrichment among top DEGs
156 (filtered by ±1.5 Log_2FC), we performed gene-ontology analyses via ClusterProfiler[29], against a
157 background of all expressed genes to avoid exclusion of biologically relevant low abundance
158 genes. 5'-Del neurons revealed a robust enrichment of terms related to neurotransmission and
159 synaptic function in iGLUT neurons, and ligand-gated anion channel activity in iGABA neurons
160 (**Supplementary Table 2**). 3'-Del neurons were enriched for terms related to neurodevelopment,
161 significant in iGABA neurons, but only nominally enriched in iGLUT neurons. DEGs were distinct
162 between genotypes (**Extended Data Fig**. **1c,d,g,h**), with different DEGs in hierarchical clustered
163 clades enriched for DNA-binding related GO terms (**Extended Data Fig. 1e,i).** Risk enrichments
164 for schizophrenia, bipolar disorder, and autism spectrum disorder[30,31] were most enriched in 5'-
165 Del iGLUT neurons and 3'-Del iGABA neurons (**Extended Data Fig. 2**).

166 To explore aberrant *NRXN1* splicing in a more complex neurodevelopmental system, we studied
167 the effect of 5'-Del and 3'-Del in organoids. We applied dorsal forebrain patterning to yield human
168 cortical organoids (hCOs) that resembled the pallium, or applied ventral forebrain patterning to
169 generate human subpallial organoids (hSOs) that resembled the subpallium (**Fig. 2e,n and**
170 **Extended Data Fig. 3a-c,h-j**)[32–34]. To stratify LOF and GOF genotypes, we confirmed exclusive
171 MT *NRXN1* isoforms in 3'-Del organoids (**Extended Data Fig. 3d-e, k-l**). We performed single
172 cell RNA-seq (n = 47,460 cells from hCOs, n= 35,563 cells from hSOs using 10x genomics) at 6
173 months, a timepoint with well characterized neural activity[33,35], and subsequently identified
174 clusters of cell-types within hCOs and hSOs (**Fig.2f,o**), without significant differences in cell
175 frequencies across pooled genotypes (quasibinomial regression model **Fig. 2g,p**). Differentially
176 expressed gene sets in hCO-glutamatergic and hSO-GABAergic clusters identified robust

177 enrichment of GO terms related to RNA splicing (from upregulated genes), and
178 neurodevelopment and synaptic function (from downregulated genes) (**Fig. 2h,i,q,r**). Taken
179 together, these results reinforce the hypothesis that perturbations in *NRXN1* splicing converge on
180 synaptic function[14,36].

181 **Patient-specific alterations in spontaneous neural activity occur with minimal changes in**
182 **passive and excitable membrane properties.**

183 To evaluate the functional consequence of *NRXN1*$^{+/-}$ deletions in iGLUT and iGABA neurons, we
184 next conducted a population-level analysis of spontaneous neuronal activity using a multi-
185 electrode array (MEA) and an examination of passive membrane properties using whole-cell
186 patch-clamp electrophysiology. Spontaneous network activity (weighted mean firing rate, wMFR)
187 in both 5'- and 3'-Del *NRXN1*$^{+/-}$ iGLUT neurons, which increased over time in a linear fashion (**Fig**
188 **3a**), was reduced by over 40% across two independent time points, at weeks post induction
189 (WPI)4 (**Fig. 3b** 5'-Del $p = 0.0005$; 3'-Del, $p < 0.0001$, 1-way ANOVA, Dunnett's test) and WPI6
190 (**Fig 3c** 5'-Del $p = 0.0129$, 3'-Del $p = 0.0069$ 1-way ANOVA, Dunnett's test). The cell capacitance,
191 membrane resistance and resting membrane potentials did not significantly differ between 5'- and
192 3'-Del cases and control iGLUT neurons (**Fig. 3d**). To examine the intrinsic excitability, we
193 compared the input-output curve for induced firing and found slightly lower firing in 5'-Del iGLUT
194 neurons, but no difference in 3'-Del iGLUT neurons (**Fig. 3e**). The voltage-dependent sodium and
195 potassium current densities were similar across 5'-Del, 3'-Del and control iGLUT neurons
196 (**Extended Data Fig**. **4a**). Taken together, these results suggest that changes in passive or
197 intrinsic excitability membrane properties cannot fully explain the reduced firing observed on
198 MEAs for 5'-Del and 3'-Del in iGLUT neurons.

199 In parallel, we generated iGABA neurons with the same 5'-Del, 3'-Del, and control hiPSCs, as
200 above. We observed that immature *NRXN1*$^{+/-}$ iGABA neurons exhibited a robust ~2-fold increase
201 in population-wide wMFR activity (~WPI2) from both 5'-Del and 3'-Del cases (5'-Del $p = 0.0029$,
202 3'-Del $p = 0.0015$ 1-way ANOVA, Dunnett's test) (**Fig. 3f,g**). Though unexpected for GABA
203 neurons, the finding is consistent with activation of ionotropic GABA receptors leading to
204 depolarization due to low KCC2 expression and high chloride levels[37]. Indeed, immature iGABA
205 neurons expressed higher (10-fold increase compared to WPI2 neurons) levels of *SLC12A5* (the
206 gene encoding *KCC2*) (**Extended Data Fig. 5a** $p < 0.0001$, 2-way ANOVA, Dunnett's test).
207 Furthermore, this transient hyperexcitability was pharmacologically inhibited by 10μM gabazine,
208 a selective $GABA_A$ antagonist (**Extended Data Fig. 5b,c**). In mature iGABA neurons (WPI6),

209 however, the average wMFR decreased in 5'-Del and 3'-Del neurons (5'-Del p = 0.0323; 1-way
210 ANOVA, Dunnett's test) (**Fig. 3h**). Like iGLUT neurons, the passive and intrinsic excitability
211 membrane properties of mature iGABA neurons were not different between *NRXN1*$^{+/-}$ 5'-Del or
212 3'-Del and controls (**Fig. 3i,j and Extended Data Fig. 4d**). Overall, these data suggest that
213 patient-specific changes in spontaneous neural activity are not fully explained by differences in
214 passive and excitable membrane properties in iGLUT or iGABA neurons from *NRXN1*$^{+/-}$ 5'-Del
215 and 3'-Del patients.

216 ***NRXN1*$^{+/-}$ 5' and 3' deletions result in divergent synaptic transmission deficits.**

217 To further dissect the factors mediating phenotypes in altered spontaneous firing, we investigated
218 the efficacy of synaptic transmission by patch-clamp electrophysiology. Voltage-clamp recordings
219 of spontaneous excitatory post-synaptic currents (sEPSCs, no TTX) in iGLUT neurons revealed
220 decreased frequency of events for both for 5'-Del and 3'-Del iGLUT neurons (**Fig. 4a**). The
221 cumulative probabilities of inter-event-intervals (IEI) for both 3'-Del (p = 4.88E-5, Levene's test
222 with Bonferroni correction) and 5'-Del iGLUTs (p = 2.54E-11, Levene's test with Bonferroni
223 correction) (**Fig. 4a,b**) was significantly increased, compared to controls. The sEPSC amplitude
224 increased for 5'-Del neurons (p = 3.88E-4, Levene's test with Bonferroni correction) (**Fig. 4a,c**).
225 Miniature excitatory post-synaptic currents (mEPSCs, +TTX) showed similar trends in IEI but no
226 changes in amplitude sizes across genotypes (IEI 5'-Del p = 0.0411, 1-way ANOVA, Dunnett's
227 test) (**Extended Data Fig. 4b,c**). These reductions in synaptic transmission are consistent with
228 the transcriptomic signatures; pre-synaptic (SynGO) genes showed a larger change (than post-
229 synaptic) in synaptic gene expression signatures (5'-Del Pre-SynGO, Log_2FC = 0.1252; 3'-Del
230 Pre-SynGO, Log_2FC= -0.0156) (**Fig. 4d,e**). We further probed transcriptional signatures of known
231 *NRXN1* trans-synaptic interaction partners that mediate synapse formation, function, plasticity
232 and are frequently linked with neuropsychiatric disease[16], and found they were represented in
233 DEGs, including *CBLN2*, *LRRTM4* and *NXPH1*, suggesting these synaptic effects are largely
234 driven by change in *NRXN1* expression (**Fig. 4f**).

235 By contrast, synaptic transmission in iGABA neurons appeared to be enhanced. The frequency
236 of spontaneous inhibitory post-synaptic currents (sIPSCs) increased, marked by a significant
237 decrease in IEI in 3'-Del iGABA neurons (p = 1.00E-4 by Levene's test with Bonferroni correction)
238 (**Fig. 4i,j)**. There was no change in sIPSC amplitude (**Fig. 4i,k**). Miniature inhibitory post-synaptic
239 currents (mIPSCs) recorded in the presence of TTX and CNQX (AMPA/Kinate receptor
240 antagonist) revealed similar trends in IEI, with no change in mIPSC amplitudes (**Extended Data**

241 **Fig. 4e,f**). Similarly, SynGO analysis revealed concordant changes in synaptic transmission and
242 transcriptomic signatures at 3'-Del (Pre-SynGO Log_2FC = 0.0324) and represented DEGs among
243 *NRXN1* trans-synaptic interaction partners *CBLN2*, *NLGN1*, *NXPH1, CASK,* and *LRRTM2-4* (**Fig.**
244 **4l-n)**.

245 Quantification of synaptic puncta (via immunostaining against synapsin-1, SYN1), normalized to
246 dendritic length (via immunostaining somatodendritic marker MAP2) uncovered a bidirectional
247 decrease in iGLUT neurons (**Fig. 4g,h**), and an increase in iGABA neurons (**Fig. 4o,p**). Thus,
248 divergent neurotransmission phenotypes appear to correlate with synapse number. Overall,
249 patient-specific alterations in spontaneous neural activity were driven by synaptic deficits, with the
250 cell type-specific impact of aberrant *NRXN1* splicing resulting in divergent neurotransmission
251 phenotypes and changes in synapse number. Furthermore, non-recurrent LOF and GOF
252 presented unequal effect sizes between cell-types, with 5'-Del neurons being most impacted by
253 excitatory transmission, but 3'-Del neurons being affected by both excitatory and inhibitory
254 transmission. Given that deletions affected iGLUT and iGABA neurons in opposing directions,
255 these findings implicate *NRXN1* as a key mediator of excitatory/inhibitory balance, a prevalent
256 theme among neuropsychiatric disorders[38].

257 **Isogenic validation of bidirectional excitatory-inhibitory (E-I) synaptic deficits.**

258 To demonstrate a direct link between aberrant *NRXN1* splicing and synaptic dysfunction, we
259 designed an experiment to specifically target splicing patterns. We utilized short hairpin RNAs
260 (shRNAs) to knockdown wildtype splice isoforms in control lines, mimicking a LOF phenotype.
261 Targeted knockdown of constitutively expressed exon 9 (expressed in alpha isoforms but not beta
262 isoforms) achieved mRNA knockdown of ~55% in iGLUT neurons, and ~75% in iGABA neurons
263 across one or more isogenic pairs (compared to a non-targeting (NT) control shRNA) (**Extended**
264 **Data Fig. 6a,e**). These knockdowns would roughly mimic a 5'-Del heterozygote. Differential
265 splicing analysis confirmed the reduction of $\beta \rightarrow \alpha$ splicing in both iGLUT and iGABA neurons by
266 ΔPSI -0.191 (p = 0.0083) and -0.208 (p = 0.0202), respectively (**Fig. 5a, i**), without significantly
267 altering other *NRXN1* splice sites. Functionally, we observed decreased synaptic transmission in
268 iGLUT neurons (i.e., increased sEPSC IEI, p = 2.2E-16 by Levene's Test) (**Fig. 5b,c**), and
269 increased synaptic transmission in iGABA neurons (decreased IEI, p = 3.65E-8 by Levene's Test
270 and p = 0.0092 by Student's t-test) (**Fig. 5j,k**), similar to the changes with 5'-Del neurons (**Fig.**
271 **4b,j**). Transcriptomic profiles of isogenic lines further validated *NRXN1* knockdown (**Extended**
272 **Data Fig 6c,g)** and demonstrated DEGs related to multiple aspects of synaptic function in both

273 iGLUT (29/258 DEGs; 1.274161-fold, p = 0.1049) and iGABA neurons (384/3525 genes;
274 1.234861-fold, p = 1.307E-6) (**Fig. 5d,i and Supplementary Table S2**). Altogether, knockdown
275 of wildtype splicing recapitulated cell-type-specific differences in *NRXN1*$^{+/-}$ 5'-Del neurons,
276 causally implicating decreased wildtype *NRXN1*α expression (LOF) as a driver of cell-type-
277 specific phenotypes.

278 For GOF *NRXN1 3*'-Del neurons, we took a different approach and applied shRNAs to knockdown
279 mutant splice isoforms, in an attempt to reverse the GOF phenotype. We designed a shRNA
280 against the mutant splice junction overlapping exons 20 and 24, expressed in all 3'-Del unique
281 *NRXN1* alpha and beta isoforms, and achieved targeted knockdown of mutant splice isoforms by
282 95% in iGLUT, and 25% in iGABA neurons in both donors (**Extended Data Fig 6b,f**). Differential
283 splicing analysis again confirmed the selective reduction of GOF splicing in both iGLUT and
284 iGABA neurons, by ΔPSI -0.108 (p = 0.0623) and -0.074 (p = 0.0258), respectively (**Fig. 5e,m**),
285 without significantly altering other *NRXN1* splice sites. In the donor with the most robust
286 knockdown in both iGLUT (90%) and iGABA (37%) neurons, electrophysiological recordings
287 revealed a reversal of synaptic transmission phenotypes, achieving IEI levels similar to control
288 iGLUT and iGABA neurons (**Fig. 4b,j**). In iGLUT neurons, shRNA MT decreased sEPSC IEI (p <
289 2.2E-16 by Levene's Test and p = 0.0194) (**Fig. 5f,g**) and in iGABA neurons increased sIPSC IEI
290 (p = 0.042 by Levene's Test) (**Fig 5h,o**), as compared to shRNA-NT. Parallel to the LOF isogenic
291 transcriptomic profiles, the GOF isogenic line had modest changes in iGLUT neurons (3/28 DEGs;
292 1.214533-fold, p = 0.4541 by Levene's test), but more pronounced synaptic DEGs in iGABA
293 neurons (128/1077 DEGs; 1.347225-fold, p = 2.694E-4) (**Fig. 5h,p and Extended Data Fig.
294 6d,h**).

295 In summary, knockdown of WT *NRXN1* in iGLUT and iGABA neurons recapitulated the
296 consequences of reduced $\beta \rightarrow \alpha$ splicing on neurotransmitter phenotypes of 5' LOF *NRXN1*
297 deletions, while knockdown of MT splicing appeared to mitigate the negative effect of the 3' GOF
298 *NRXN1* deletions. Furthermore, the bidirectional effect of *NRXN1* deletions on iGLUTs
299 (decrease) and iGABAs (increase), i.e., E-I balance, was reversed by shRNA treatments.
300 Transcriptomic profiling of shRNA treated isogenic lines revealed ~10% of DEGs related to
301 synaptic function across all four experimental conditions. Altogether, shRNA mediated
302 perturbations among WT and MT isoforms causally implicate *NRXN1* splicing to synaptic
303 dysfunction.

304 **Framework for precision medicine against stratified LOF/GOF phenotypes**

305 As a proof-of-principle therapeutic intervention, we tested methods to directly and indirectly
306 manipulate *NRXN1* expression, separately targeting LOF and GOF mechanisms, and focusing
307 on reversing decreased excitation phenotypes in iGLUT neurons.

308 For LOF patients, we hypothesized that increasing transcription of the WT *NRXN1α* allele would
309 restore *NRXN1* levels and reverse the signature of reduced β→α splicing (**Fig. 6a**). β-estradiol
310 reversed *NRXN1* LOF neurogenesis deficits in *xenopus* and human NPC models[39]. Although the
311 mechanism is unknown, chromatin immunoprecipitation with sequencing (ChIP-Seq) in mouse
312 brain tissue identified estrogen receptor alphaα (ERα) binding sites at the *NRXN1* alpha locus
313 (**Extended Data Fig. 7a,b**)[40]. We predicted *NRXN1* to be a target of ERα, and report that acute
314 treatment with β-estradiol (10nM or 30nM, 3-5 days) significantly increased *NRXN1α* expression
315 in iGLUT neurons (p = 0.0297 by Student's t-test) derived from 5'-Del patients (**Fig. 6b**), but not
316 in controls (**Extended Data Fig. 7c**). The functional effect of chronic treatment of post-mitotic 5'-
317 Del neurons with 30nM β-estradiol (relative to DMSO vehicle) was evaluated across spontaneous
318 neural activity (MEA), synaptic transmission (patch-clamp) and gene expression (RNA-
319 sequencing). MEA recordings at WPI3 revealed a significant increase in wMFR activity (p =
320 0.0057 via student's t-test) in the β-estradiol treated condition (**Fig. 6c**). Transcriptional profiling
321 of the β-estradiol treatment detected an inversion of the β→α splicing signature (ΔPSI 0.045), and
322 more subtle changes in global gene expression (7 upregulated and 34 downregulated DEGs)
323 (**Fig. 6d,e**). Likewise, patch-clamp recordings revealed that β-estradiol treatment ameliorated the
324 sEPSC IEI phenotype in 5'-Del neurons (p = 4.62E-4 by Levene's Test, Bonferroni corrected),
325 but not in vehicle treated 5'-Del neurons (p = 0.9055 by Levene's Test), compared to healthy
326 controls (**Fig. 6f,g**).

327 Towards a therapeutic strategy for treating GOF patients, we investigated the utility of anti-sense
328 oligonucleotides (ASOs), recently used to treat several neurological diseases[41], to target a
329 specific RNA splice site. We designed an "alternative splice matrix" by juxtaposing splice donor
330 and acceptor RNA sequences from each *NRXN1α* exon, generating all possible combinations of
331 canonical and non-canonical splice junctions (**Fig. 6h,i**). Then, for the sequence covering the
332 20/24 mutant splice junction, we designed an ASO to facilitate targeted RNAseH1-dependent
333 degradation of 3-Del mutant isoforms. ASO treatment (1μM) for 72hrs decreased total mutant
334 isoforms by ~55% in iGLUT neurons (p < 0.001 by student's t-test), as compared to a non-
335 targeting control ASO (**Fig. 6j**). Differential splicing analysis confirmed the reduction of GOF
336 splicing (ΔPSI -0.103) and increased ratios of SS4+. We also observed a significant reduction in

337 β→α splicing (ΔPSI -0.253, p = 0.007, Bonferroni corrected), perhaps resulting from reduced MT
338 isoform expression, contrasting the elevated baseline of *NRXN1α* in 3'-Del (**Fig. 6k**).
339 Transcriptomic profiling revealed robust DEGs, enriched for synaptic properties, neurotransmitter
340 signaling, and neurodevelopmental pathways **(Supplementary Table S3)** (231/1844 Bonferroni
341 corrected DEGs annotated in SynGO; 1.420028-fold, p = 1.016E-08), (**Fig. 6c-d**). To demonstrate
342 the broader applicability of an ASO strategy, we report mutant splice isoforms in post-mortem
343 brain tissue from an unrelated *NRXN1*$^{+/-}$ case diagnosed with autism spectrum disorder (ASD)
344 (**Supplemental Fig. 8**). By integrating long-read and short-read sequencing[15], we identified nine
345 high-confidence isoforms that are predicted to be translated: two of which contained a novel splice
346 junction overlapping the deletion encompassing exon 14/19, targetable by an ASO tailored to the
347 mutant splice junction.

348 Altogether, increased *NRXN1* expression in LOF neurons and knockdown of mutant splicing in
349 GOF neurons can each rescue the splicing defects that produce opposing cell-type-specific
350 case/control differences in *NRXN1*$^{+/-}$ neurons. We propose the aberrant *NRXN1α* splicing is a key
351 a driver of complex *NRXN1*$^{+/-}$ phenotypes and that modulators of *NRXN1* expression and/or
352 splicing represent novel targeted therapies.

353 **DISCUSSION**

354 *NRXN1*$^{+/-}$ deletions are non-recurrent between patients, linked to diverse clinical outcomes that
355 cannot be explained by the size or boundaries of the deletion itself[6]. Here, we show that *NRXN1*
356 splicing alters excitatory-inhibitory (E-I) imbalance[1,32], a common theme among neuropsychiatric
357 disorders, by bidirectionally regulating synaptic transmission, with a decrease in frequency of
358 sEPSCs in 5'-Del and 3'-Del iGLUT neurons but an increase in frequency of sIPSCs in 3'-Del
359 iGABA neurons. Using a case/control *NRXN1*$^{+/-}$ cohort as well as isogenic manipulations of the
360 *NRXN1* isoform repertoire, we report distinct phenotypic effects in human iGLUT and iGABA
361 neurons that predominately manifest in changes in the frequency of synaptic function. These
362 results suggest causal relationships between aberrant *NRXN1* splicing and synaptic dysfunction,
363 dictated by unique patient-specific mechanisms.

364 The regulation of *NRXN1* splicing, including the formation of aberrant splice sites by specific
365 RBPs, is poorly understood; >100 RBPs are predicted to interact with *NRXN1* mRNA in a cell-
366 type[42,43] and neuronal activity[23] dependent-manner. For example, KH-domain STAR-family
367 RBPs regulate SS4+ in a neuronal activity dependent manner[23–25], mediating trans-synaptic

368 signaling by varying interactions among a host of post-synaptic ligands. Although patient
369 transcriptomic profiles nominate STAR proteins as potential drivers of aberrant GOF splicing,
370 further investigation is required to identify the biochemical mechanisms involved. Nevertheless,
371 we posit that direct manipulation of splicing may achieve therapeutic benefit in some cases.

372 Neurexins are expressed across all synapses and among certain non-neuronal cell-types, such
373 as astrocytes, perhaps with distinct cell-type-specific functional roles[37]. Mechanistically, our study
374 did not resolve whether mutant GOF isoforms shifted the stoichiometry of alternative splicing
375 against wildtype RNA isoforms or if they altered trans-synaptic protein-protein interactions. In
376 either case, *NRXN1* encodes a pre-synaptic molecule but traditional neuropharmacological
377 agents typically target specific receptors. Given that patient-specific patterns of aberrant *NRXN1*
378 splicing across non-recurrent mutations are unlikely to be reversed by a pharmacological
379 approach, precision therapies that target aberrant splicing are needed to effectively reverse
380 defects in the multiple cell types affected by patient-specific deletions.

381 The opposing effects of $NRXN1^{+/-}$ in glutamate and GABA neurons provides the foundation for
382 evaluating proof-of-concept therapeutics that target distinct LOF or GOF mechanisms. For LOF
383 mutations, mechanisms for upregulation of wild-type allelic expression and/or restoration of
384 proper *NRXN1* splicing are required (**Fig. 6a**). While direct approaches to increase *NRXN1*
385 expression may be ideal, such as small activating RNAs[44], further work is required to carefully
386 evaluate safety and efficacy in clinical trials. On the other hand, indirect approaches have the
387 advantage of prioritizing drugs from a list of already clinically approved molecules, selected based
388 on their predicted ability to alter the expression of a target gene (e.g., LINCs[45]). With relevance to
389 the ability of estradiol to increase *NRXN1* and rescue synaptic deficits, steroid-based
390 pharmaceuticals are already used to treat neuroinflammation-related conditions[46], with recent
391 studies revealing estrogen-mediated roles in neuroprotection[39], demonstrating the safety and
392 feasibility of this approach. For GOF, ASOs designed to target a mutant splice junction and
393 facilitate degradation of MT isoforms may represent a viable therapeutic approach (**Fig. 6h**). Not
394 all in-frame coding mutations will be GOF; for example, unique mutations at non-canonical splice
395 donor/acceptor sites will require further characterization prior to assigning LOF/GOF status. In all
396 cases, maintaining a stoichiometric balance between MT and WT isoforms may require
397 combination treatments (e.g., ASO and transcriptional activator) for therapeutic benefit. Cases of
398 muscular dystrophies treated via splicing modulating ASOs have proven effective[47], but overall,
399 gene therapy in brain disease has shown mixed successes[48]. Critically, although our proof-of-
400 principle *in vitro* findings suggest a novel therapeutic avenue, translational studies will be required

401 to confirm the efficacy of this framework *in vivo*, and ultimately, in the clinic.

402 Several technical limitations warrant acknowledgement. The iGLUT and iGABA neuron
403 populations studied herein are not just immature, but also comprise diverse neuronal subtypes[49];
404 thus, the more discrete impacts of *NRXN1*$^{+/-}$ on synaptic physiology across different subtypes of
405 neurons (e.g., SST versus PV expressing GABA neurons) remain unresolved. Moreover, future
406 studies in more physiologically relevant and circuit-like models may uncover novel non-
407 autonomous and activity-dependent phenotypes. Mechanistically, it will be important to probe the
408 biochemical and proteomic interactions of *NRXN1*; for example, unbiased proximity-labelling
409 methods (e.g., BioID[50]) could define perturbations in protein-protein interaction profiles between
410 wildtype and mutant isoforms.

411 Precision medicine seeks to tailor treatments to individual patients,[51] regardless of differential
412 penetrance of genetic mutations. Therefore, we focused on stratifying mutations in the same gene
413 based on LOF and GOF mechanisms, in contrast to clinical diagnosis (bipolar disorder or
414 schizophrenia), with the goal of one day providing the right therapy at the right time to the right
415 patient. The most successful examples of precision medicine to date have been in cancer[52] and
416 monogenic disease[53], whereby genetic analyses revealed molecular subtypes that benefited from
417 specific treatments. In the context of brain disorders, patient stratification is particularly
418 challenging, reflecting in part the myriad rare and common variants linked to disease[54]. Disease-
419 agnostic analyses reveal that transcription factors and nucleic acid binding proteins are
420 overwhelmingly driven by LOF mutations, whereas signaling molecules, enzymes, receptors and
421 transporters more frequently incur dominant GOF mutations[55]. When both are possible, distinct
422 mutations in the same genes can result in pleiotropic phenotypic effects. A binary therapeutic
423 approach, similar to what we proposed here for *NRXN1*, may prove suitable for dual LOF an GOF
424 mechanisms linked to mutations in other neuropsychiatric disorder-related synaptic genes (e.g.,
425 *NLGN3*[56], *CACNA1D*[57], *CACNA1C*[58], *SCN1A*[59], *SCN2A*[60]) as well as broadly in
426 neurodegenerative disease (e.g., *SOD1*[61], *TDP43*[61], *FUS/TLS*[61], *C9ORF72*[62], *AR*[63]), and many
427 short tandem repeat disorders[64]. Taken together, our work advances precision medicine,
428 demonstrating the necessity of functionally dissecting the phenotypic impact of diverse patient-
429 specific genetic variants across cellular contexts, in order to resolve candidate therapies across
430 stratified disease mechanisms.

431 **METHODS**

432 *Plasmid designs and molecular cloning*

433 *i. TetO-Ascl1-Neo*

434 The *ASCL1* insert from TetO-Ascl1-Puro (Addgene #97329) was synthesized as a gBLOCK
435 flanked by EcoR1 cut sites, and cloned into TetO-hNgn2-Neo using EcoR1 to remove *NGN2.* The
436 recipient vector was dephosphorylated with shrimp alkaline phosphatase (rSAP NEB #M0371S)
437 during the digest, column purified and ligated at a 1:1 vector to insert ratio using the QuickLig Kit
438 (NEB #M2200S). The *ASCL1* stop codon was subsequently mutated using the QuickChange II-
439 XL site-directed mutagenesis kit (Agilent #200523) and verified via whole plasmid sequencing
440 from plasmidsaurus.

441 *ii. shRNA RNA interference constructs*

442 All shRNAs were designed and produced by Sigma-Aldrich via custom submitted sequences
443 against wildtype *NRXN1α* (constitutively expressed exon 9) and mutant *NRXN1α* (mutant 20/24
444 splice junction) cloned into TCR2 pLKO.5-puro.

445 *Cell Culture*

446 *i. hiPSC culture*

447 Passage matched (±3) human induced pluripotent stem cells (hiPSCs) were cultured in StemFlex
448 media (Life technologies #A3349401) on Matrigel (Corning, #354230). At ~70-80% hiPSCs were
449 clump passaged using 0.5mM EDTA in PBS without Mg/Ca (Life technologies #10010-031). Cells
450 were washed once and incubated for 4-7 min with 0.5μM EDTA at RT. The EDTA was aspirated,
451 and the remaining colonies were lifted off with 1mL of StemFlex and re-distributed at varying
452 densities in a 6–well maintenance plate. hiPSC lines were split every 4-6 days. For
453 neuronal/organoid differentiation, wells of similar confluence across all hiPSC donors were
454 resuspended and seeded onto a Matrigel coated 10cm dish and expanded until ~70-80%
455 confluency.

456 *ii. HEK293T culture and lenti-viral production*

457 HEK293T cells were maintained in 15cm dishes and cultured in DMEM supplemented with 10%
458 standard FBS (Life technologies #16000069). 3rd Gen lenti-viral particles were produced using

459 previously described methods and REV, MDL and VSV-G plasmid ratios[18], each transfected with
460 PEImax (Polysciences #24765-1). Each PEIMax batch was volumetrically titrated at total µgDNA:
461 µLPEI for optimal transfection efficiency.

462 *iii. Primary mouse glia production*

463 All mouse work was performed under approved IACUC protocols at the Icahn School of Medicine
464 at Mount Sinai. C57BL/6 mice were used as breeding pairs. For glial preps, dissected cortices
465 from 3 pups (at p0-3) were dissociated using papain (R&D #LS003126) and plated on 10cm
466 dishes in MEF medium (DMEM, 10% Cosmic Calf Serum (Fisher #SH3008703HI), 1x Antibiotic-
467 antimycotic (Life technologies #15240), 1x Sodium Pyruvate (Life technologies #11360070), 1x
468 MEM Non-Essential Amino Acids Solution (Life technologies #11140050), 4uL 2-Mercaptoethanol
469 (Sigma #60-24-2), supplemented with 100µg/mL Normocin (InvivoGen #ant-nr-2). Glial cells were
470 recovered and propagated for 7 days, and expanded into three 10cm dishes. To promote neuronal
471 health and synapse maturation, we utilized mouse glia from well-established protocols that
472 significantly outperform human astrocytes for co-culture experiments[19,21,65]. All glial preps were
473 tested twice for mycoplasma (Normocin withdrawn) (Lonza, #LT07-318) prior to freezing or
474 neuronal co-culture. At day 14, one 10cm dish with mouse glia were distributed to two MEA, 12-
475 or 24- well plates, and subsequently inactivated with 4µM Ara-C (Sigma #C1768) prior to or during
476 re-seeding of induced neurons.

477 *iv. iGLUT induction and astrocyte co-culture*

478 At day -1 hiPSCs expanded in 10cm dishes were dissociated with accutase (StemCell
479 Technologies, #07920), washed and pelleted with a 1:4 ratio of accutase to DMEM for 5 min at
480 1000 rcf, and re-suspended with StemFlex media containing ROCK inhibitor, THX (10µM/mL;
481 Sigma Aldrich, SML1045). The hiPSCs are then co-transduced with TetO-Ngn2-Puro (Addgene
482 #79049) or TetO-Ngn2-Neo (Addgene# 99378) and UCb-rtTA (legacy vector from the lab of Fred
483 Gage) and seeded at 1.0-1.5x10^6 cells in 1.5mL per well on 6-well plates were coated with 2x
484 Matrigel for at least one hour at 37°C. The hiPSC-viral mixture was then incubated overnight. The
485 following morning (day 0), a full media change with iGLUT induction media was performed with
486 the following recipe: Neurobasal Media: 1x N2 (Life technologies #17502-048), 1x B-27 minus
487 Vitamin A (Life technologies #12587-010), 1x Antibiotic-Antimycotic, 1x Sodium Pyruvate, 1x
488 GlutaMax (Life technologies #35050), 500µg/mL cyclic-AMP (Sigma #D0627), 200µM L-ascorbic
489 acid (Sigma #A0278), 20ng/ml BDNF (Peprotech #450-02), 20ng/ml GDNF (Peprotech #450-10),

490 1µg/ml natural mouse laminin (Life technologies #23017015). On days 1-2, iGLUT cells were
491 treated with respective antibiotic concentrations at 1µg/mL puromycin (Sigma# P7255) or
492 0.5µg/mL neomycin (Life technologies #11811-031). On day 3, antibiotic medium was withdrawn
493 and iGLUT cells were treated with 4µM Ara-C. On Day 4, iGLUT cells were dissociated with
494 accutase for 15 min, washed and pelleted with a 1:4 ratio of accutase to DMEM for 5 min at 800
495 rcf, and re-suspended with iGLUT media containing ROCK inhibitor, Ara-C and 2% low-
496 hemoglobin FBS (R&D systems #S11510). iGLUT neurons were distributed among wells (500-
497 750k cells per 24wp or 0.75-1.5E6 cell per 12wp) pre-seeded with confluent mouse glia. The
498 following day, iGLUT neurons received a full media change with Brainphys maturation media
499 (Neurobasal Media, 1x N2, 1x B-27 minus Vitamin A, 1x Antibiotic-Antimycotic, 500µg/mL cyclic-
500 AMP, 200µM Ascorbic Acid, 20ng/ml BDNF, 20ng/ml GDNF, 2% low-hemoglobin FBS, 1µg/ml
501 Mouse Laminin) supplemented with Ara-C and were subsequently monitored for growth of non-
502 neuronal/glial cells. Ara-C treatment was tittered down with half-media changes (without Ara-C)
503 every 3-4 days until used for experiments.

504 *v. iGABA induction and astrocyte co-culture*

505 iGABA production paralleled the methods aforementioned. hiPSCs were instead co-transduced
506 with TetO-Ascl1-puro (Addgene #97330) or TetO-Ascl1-neo (Addgene #TBD), TetO-Dlx2-hygro
507 (Addgene #97329) and UCb-rtTA and seeded at 0.8-1.2x10^6 cells in 1.5mL per well on 6-well
508 plates similarly prepared. The following morning (day 0), a full media change with iGABA induction
509 media (DMEM/F-12 + Glutamax, 1x N2, 1x B-27 minus Vitamin A, 1x Antibiotic-Antimycotic) was
510 performed. On days 1-2 iGABA cells were selected with respective antibiotic concentrations at
511 1µg/mL puromycin or 0.5µg/mL neomycin and 0.25µg/mL hygromycin (Life Technologies
512 #10687010), followed by antibiotic withdrawal and Ara-C treatment on day 3. iGABA neurons
513 were re-seeded identically to iGLUT cells, at 150-250k cells per 24wp well. iGABA cultures were
514 morphologically QC'ed prior to all experiments, with uncharacteristic batches being discarded.

515 *vi. Cortical and subpallial organoid differentiation*

516 Cortical organoids were generated according to the protocol described by Sloan et. al.[66], with
517 several modifications. hiPSCs were first aggregated into embryoid bodies (EBs) using an
518 AggreWell™800 Microwell Culture Plate system (Stemcell Tech #34850). Expanded hiPSCs
519 were rinsed twice with DPBS without Ca/Mg, and then dissociated using accutase. 3x10E6
520 hiPSCs were added to a single well in the prepared AggreWell and allowed to aggregate in a

521 37°C incubator for 24 hours. The following day (day 0), EBs were dislodged from the AggreWell
522 plate using a cut p1000 pipette tip and passed over a 40µm strainer, and washed with excess
523 DMEM. The strainer was inverted over an Ultra-Low Attachment 10 cm culture dish and the EBs
524 were collected in spheroid induction media, which contained Stemflex supplemented with two
525 SMAD inhibitors, SB-431542 (SB) and LDN193189 (LDN), and THX. The following day (day 1),
526 the media THX was withdrawn. From d2-d6, induction media was replaced daily, and no longer
527 contained the Stemflex supplement (only base Stemflex media with SB and LDN). On day 6, the
528 media was replaced with organoid patterning media, formulated with Neurobasal-A medium, 1x
529 B-27 minus Vitamin A, 1x GlutaMAX, and 1x Antibiotic-Antimycotic. From d6-d24, organoid
530 maturation media was supplemented with 20ng/ml of EGF (R&D Systems, #236-EG) and 20ng/ml
531 FGF2 (R&D Systems, #233-FB-01M). Media was changed every day from d6 – d15, after which
532 media was changed every other day. From d25-d43, the organoid maturation media was
533 supplemented with 20ng/ml of NT-3 (PeproTech, #450-03) and 20ng/ml BDNF. From d43
534 onwards, organoids received organoid maturation media with no supplements, and media was
535 changed every 4 days or as needed. Subpallial organoids were generated in the same way as
536 cortical organoids, but with additions in media formulations. From d4-d23, hSOs received
537 spheroid induction media or organoid maturation media supplemented with 5µM of the Wnt
538 inhibitor, IWP-2 (Selleckchem, #S7085). From d12-d23, hSO organoids received neuronal
539 differentiation media supplemented with 100nM of the SHH agonist, SAG (Selleckchem, #S7779).

540 *Electrophysiology*

541 *i. Multi-electrode array (MEA)*

542 The Axion Maestro (Middleman) system was used to perform all MEA recordings. Following
543 iGLUT and iGABA inductions, 80-100k cells were re-plated on each MEA well and measurements
544 began as early as DIV9 for both iGLUT and iGABA co-cultures. For time course experiments,
545 MEA plates were recorded every 2-3 days per week with a full media change prior to each
546 recording. Comparisons for iGLUT neurons were made at WPI4 and WPI6, as well characterized
547 timepoints for synaptic activity. For iGABA neurons, comparisons were made at WPI2 and WPI6
548 to include both timepoints of elevated neuronal activity. For acute drug treatments with gabazine
549 (Tocris, #1262), a baseline recording (pre-treatment) was first obtained, followed by an immediate
550 addition of a small volume of concentrated stock. A second, post-treatment recording was then
551 obtained to evaluate the difference in activity before and after drug treatment. A full media change
552 was performed one day prior to the day of recording. MEA wells were visually QC'ed for similar

553 densities prior to recording, with high/low density wells being excluded from recordings.

554 *ii. Whole-cell patch-clamp electrophysiology*

555 For whole-cell patch-clamp recordings, iGLUT (300k/well) or iGABA (250k/well) human-mouse
556 glia co-cultures were recorded at 4-6 weeks following dox-induction (time points specified in figure
557 legends), with a full media change one day prior to recording. Only coverslips with similar densities
558 were selected for recording. Cells were visualized on a Nikon inverted microscope equipped with
559 fluorescence and Hoffman optics. Neurons were recorded with an Axopatch 200B amplifier
560 (Molecular Devices), digitized at 10 kHz using a Digidata 1320a (Molecular Devices) and filtered
561 between 1-10 kHz, using Clampex 10 software (Molecular Devices). Patch pipettes were pulled
562 from borosilicate glass electrodes (Warner Instruments) to a final tip resistance of 3-5 MΩ using
563 a vertical gravity puller (Narishige). To sustain the baseline activity of neurons from extended
564 cultures, coverslips were recorded in base Brainphys medium (external solution, Osm 305, pH
565 7.49). Each coverslip was equilibrated to room temperature for 10min, with 3-5 neurons were
566 recorded for no more than a total of 75min per coverslip. For measurements of passive and
567 excitable properties, an internal patch solution was used containing (in mM): K-d-gluconate, 140;
568 NaCl, 4; MgCl2, 2; EGTA, 1.1; HEPES, 5; Na2ATP, 2; sodium creatine phosphate, 5; Na3GTP,
569 0.6, at a pH of 7.4. Osmolarity was 290-295 mOsm. Neurons were chosen at random using DIC
570 and all recordings were made at room temperature (~22°C). Current-clamp measurement
571 occurred across -10pA to +50pA steps, with a maximum stimulus of +60pA, whereas voltage-
572 clamp measurements occurred across -50mV to +50mV steps, normalized to cell capacitance (to
573 control for variable neuronal size). Current clamp measurements were corrected for the junction
574 potential (~-15.5mV). For sEPSC/sIPSC recordings, the internal solution was replaced with (in
575 mM): Cesium-Chloride, 135; HEPES-CoOH, 10; QX-314, 5; EGTA, 5. Osmolarity was 290-295
576 mOsm. All mEPSC measurements were recorded under the presence of 100nM TTX-citrate
577 (Tocris Cat# 1069). mIPSC measurements were made using 100nM TTX-citrate and CNQX-
578 disodium salt (Tocris Cat#1045/1) to pharmacologically inhibit ionotropic glutamate receptors. All
579 chemicals were purchased from Sigma-Aldrich Co. (St. Louis, MO). All toxic compounds were
580 handled in accordance with ISMMS EHS standards.

581 *iii. Patch-clamp data analysis*

582 All patch-clamp data were analyzed on Clampfit (v11) and Easy-Electrophysiology (v2.4.1 or beta-
583 versions). Briefly, for voltage-clamp data, files were opened in Easy-Electrophysiology and two

584 bins were assigned for Na+/K+ measures for minimum and maximum current values, respectively.
585 For current-clamp data, files were opened in Easy-Electrophysiology and action potential (AP)
586 analysis was used to automatically determine spike number and properties. For gap-free
587 recordings, all data was post-hoc adjusted to a baseline of zero on ClampFit, and subsequently
588 analyzed in Easy-Electrophysiology by template and linear threshold detection. For case v. control
589 experiments, a minimum cutoff of 10 events for the duration of the recording (3min) was used as
590 QC. For typical EPSC events, a single template from a randomly chosen recording was used to
591 analyze all traces (with a 30ms decay cutoff). For IPSC events, three templates were used to
592 detect variable GABA receptor kinetics, for all traces (with a 60ms decay cutoff). An amplitude cut
593 off of 7pA was used to call positive events. For cumulative probabilities, each cell was binned by
594 experiment and averaged across all cells for a representative curve (GraphPad Prism).

595 *RNA-Sequencing and bioinformatic analyses*

596 *i. Bulk RNA sequencing and DEG analysis of iGLUT and iGABA neurons*

597 iGLUT (DIV21) and iGABA (DIV14 or DIV35) co-cultured with primary mouse glia (to match
598 functional experiments) were harvested in Trizol and submitted to the New York Genome Center
599 for high-throughput RNA extraction and quality control, library prep using the Kapa Hyper library
600 prep with ribo-erase (Roche #KK8541) and subsequently sequenced on Illumina NovaSeq.
601 Similarly, shRNA samples were harvested at DIV21-24, and DIV35-49 for iGLUT and iGABA
602 neurons, respectively. Returned raw data files were first processed to remove mouse reads in the
603 RNA-seq data, a combined genome reference (hg38 and mm10) was created using the "mkref"
604 command in cellranger (v6.1.2). The raw sequencing reads were then aligned to the combined
605 genome reference using STAR (v2.7.2a)[67]. Reads that mapped specifically to the human
606 reference genome were extracted from the resulting BAM files for subsequent gene expression
607 analysis. Gene-level read counts were obtained using the Subread (v2.0.1) package
608 featureCount[68], and RPKM values were calculated using the R package edgeR[69]. To confirm
609 sample identity, variants were called from RNA-seq bam files by HaplotypeCaller and
610 GenotypeGVCFs in GATK (v4.2.0). Then bcftools (v1.15) was used
611 to examine variants concordance with variants from whole-exome sequencing data from the
612 same donor. Following donor identity confirmation, the differential gene expression analysis
613 followed the methods as described previously[70]. First, CibersortX[71] was utilized to predict
614 differences in cell type composition across all samples. The R package variancePartition
615 (v1.30.2)[72] was then employed to investigate the contribution of specific variables to the variance

616 in gene expression. The limma/voom package[27] was used for differential expression analysis,
617 with the regression of fibroblast and hiPSC cell type compositions. The analysis began with a
618 comparison between the case and control groups. Subsequently, within each case vs control
619 group, subgroup comparisons were conducted for all four pairs (two donors each for 3'-Del and
620 5-Del patients and two healthy controls) of samples, accounting for heterogeneity between
621 different donors. Genes with an FDR less than 0.1, and a fold change above 1.5 and below -1.5
622 in all four pairs of subgroup comparisons were defined as the final set of differentially expressed
623 genes, unless otherwise specified. Kallisto (v0.46.1)[73] was used to calculate the *NRXN1* exon
624 usage ratios.

625 *ii. Analysis of alternative splicing estimates via LeafCutter*

626 Reads were aligned to a combined GRCh38 human and GRCm38 mouse reference genome
627 using STAR (v2.7.1.a), with an index built against GRCh38 Gencode GTF (v92) using the option
628 -sjdbOverhang 100. To allow the discovery of novel splice junctions and increase mapping
629 accuracy, STAR was run in two-pass mode with standard options. Reads mapping exclusively to
630 GRCh38 were subsequently extracted and replicates merged with samtools (v1.6). Splice
631 junctions were extracted from the resulting bam files with regtools v0.5.2 `junctions extract` with
632 parameters "-a 8", "-m 50", and "-M 1200000" due to potential for the genomic deletions to cause
633 larger intervals between junctions. Junctions were clustered using the leafcutter pipeline
634 (v2c9907e) script "leafcutter_cluster_regtools.py" with option "-l 1200000". For differential splicing
635 analysis, leafcutter was run with "-i 2 -g 0" to reflect the samples used. Splicegraph visualizations
636 were constructed using a modified version of the leafviz pipeline. All statistical tests utilized a
637 Dirichlet-multinomial generalized linear model, and were corrected for multiple comparisons when
638 necessary via Bonferroni adjustment.

639 *iii. Pathway and Network Analysis of DEGs*

640 For hierarchical clustering of DEGs based on gene expression fold change, the Pheatmap
641 function in R was used cluster gene expression fold change of DEGs combined from both 5'-Del
642 and 3'-Del conditions. R package clusterProfiler[29] was used to performed the gene set enrichment
643 analysis (GSEA). For each cell type, ranked gene expression of each genotype (5'-Del or 3'-Del)
644 against control were used as background and DEGs from both genotypes (5'-Del and 3'-Del) were
645 used as query gene sets. For Gene Ontology (GO) enrichment analysis, the enrichGO function
646 within R package clusterProfiler was used. For GO with a default background, query gene list was

647 converted from ‘ENSEMBL’ format to ‘ENTREZID’ format by bitr function in clusterProfiler and the
648 OrgDb parameter was set as ‘org.Hs.eg.db’. When customized genes were used as background,
649 both background and query gene lists were kept as ‘ENSEMBL’ format. For SynapseGO (SynGO
650 v1.2), DEG or prioritized DEG lists (Log_2FC filtered) gene lists were tested for enrichment with
651 "brain expressed" background set selected, containing 18035 unique genes in total of which 1591
652 overlap with SynGO annotated genes. Sunburst plots were exported via the web-based
653 application. The ASD, BP, and SCZ risk gene lists were extracted from previously curated gene
654 lists[30], Genes with the top 200 smallest FDR values and a fold change larger than 1.5 in the case
655 vs control comparison were selected for the protein interaction network analysis. Then,
656 overlapping genes between the selected gene list, the disease risk gene sets, and the proteins in
657 the SIGNOR database were utilized to query the SIGNOR database and build the interaction
658 network, using the "connect + add bridge proteins" search mode in The SIGNOR Cytoscape App
659 (v1.2)[74].

660 *v. Dissociation and 10x Single-Cell RNA sequencing of organoids*

661 Whole organoids were dissociated to the single cell level in preparation for single-cell RNA
662 sequencing using the Papain Worthington Kit (Worthington, LK003150). All solutions included in
663 the kit were prepared according to the manufacturer’s instructions. 4-6 organoids were transferred
664 to one well of a low attachment 6 well plate and were washed with PBS without Ca^{2+} and Mg^{2+}.
665 Organoids were cut with a small scalpel into smaller pieces for easier dissociation. 800µl of papain
666 solution (supplied in the kit) was added per well. Samples were incubated at 37°C for about two
667 hours or until single cell suspension was achieved. Every 15 minutes, the mixture was pipetted
668 up and down with a cut P1000 pipette tip. Once single cell suspension was reached, 500 µl of
669 inhibitor solution (supplied in the kit) was added to the well. The solution was gently mixed, filtered
670 through a 70µm-pore sieve, and transferred to a 15 ml centrifuge tube. The cells were pelleted by
671 centrifugation at 300 x g for 5 minutes at room temperature. Cell pellets were resuspended in
672 500µl of ice-cold 0.04% BSA diluted in PBS without Ca^{2+} and Mg^{2+}. scRNA-seq was performed
673 on 4-6 pooled 6-month-old organoids per donor line, per condition (hCS or hSS) for a total of 48
674 organoids. A minimum of 10,000 dissociated cells were submitted for sequencing. The library was
675 prepared using the Chromium platform (10x Genomics) with the 3’ gene expression (3’ GEX)
676 V3/V3.1 kit. Libraries were sequenced on an Illumina NovaSeq sequencer with an S4 flow cell,
677 targeting a minimum depth of 20,000 reads per cell. The lengths for read parameters Read 1, i7
678 index, i5 index, and Read 2 were 100, 8, 0, 100, respectively.

679 *vi. Bioinformatic analysis of scRNASeq data*

680 The raw sequencing data, represented as base call (BCL) files produced by the Illumina
681 sequencing platform, were subjected to demultiplexing and subsequent conversion into FASTQ
682 format using CellRanger software (version 6.0.0, 10x Genomics) with default parameters. The
683 software then mapped the FASTQ reads to the human reference genome (GRCh38) with default
684 parameters. Following this, the 'count' command in the Cell Ranger (v6.0.0) software was utilized
685 for the quantification of gene expression. For alignment and counting, the reference genome
686 refdata-gex-GRCh38-2020-A was used, which was procured from the official 10x Genomics
687 website. We performed QC and normalization using the Seurat (v3) R package[75]. For QC, we
688 filtered out low-quality cells using the following criteria: (i) cells with unique gene counts outside
689 the range of 200 to 6000; (ii) cells with more than 30% mitochondrial gene content; and cells with
690 less than 2000 unique molecular identifiers[76,77]. Post QC, we carried out normalization, scaling
691 the gene expression measurements for each cell by the total expression, multiplied by a scale
692 factor (10,000 by default), and log-transformed the results. We extracted the expression profiles
693 of the 338 genes identified by Birey et al[33], to reduce the dimensionality of the dataset through
694 principal component analysis (PCA), and identify statistically significant PCs using a JackStraw
695 permutation test. This was followed by non-linear dimensional reduction using the UMAP (Uniform
696 Manifold Approximation and Projection) technique for visualization. Cells were clustered based
697 on their PCA scores using the Shared Nearest Neighbor (SNN) modularity optimization-based
698 clustering algorithm in Seurat. After dimensionality reduction, we used known marker genes to
699 guide the clustering of cells. Each cluster was then annotated using cell type markers identified
700 by Birey et al[33]. To account for variability among individual donors we pooled genotypes, similar
701 to our strategies in all other experiments, and performed a quasibinomial regression model to test
702 if cell frequencies significantly differed between genotypes. Finally, we conducted differential
703 expression analysis across the defined cell clusters using the FindAllMarkers function in Seurat,
704 which employs a Wilcoxon Rank-Sum test to control for the variability within and between groups.
705 The significantly differentially expressed genes were then used to interpret the biological
706 significance of cell clusters. For each identified cell type, we conducted an enrichment analysis
707 using the WebGestalt (WEB-based GEne SeT AnaLysis Toolkit) online tool, with the Human
708 genome (GRCh38) as the reference set, employing a hypergeometric statistical method and the
709 Benjamini & Hochberg method for multiple test adjustment.
710

711 *vii. Analysis of ChIP-sequencing data from β-estradiol treated rodent brains.*

712 Tracks in bigWig format were downloaded from the GEO dataset GSE144718[40]. Two peaks within
713 the *NRXN1* gene region in the mm10 genome were visualized using Spark (v2.6.2)[78]

714

715 *viii. Generation of long-read sequencing data from post-mortem brain tissue*

716 All aspects of sample processing (tissue handing, RNA extraction, library prep, QC, sequencing
717 and bioinformatic analysis) was performed as previously described[15].

718

719 *Therapeutic Treatments of iNeurons*

720 *i. β-estradiol treatment*

721 β-estradiol was reconstituted in DMSO and subsequently diluted in Brainphys maturation media
722 for a final concentration of 10 or 30nM. Neurons were treated for 3-5 consecutive days, with fresh
723 drug or vehicle control replenished daily (in half media changes). iGLUT and iGABA neurons were
724 treated starting from ~DIV14-18. On the final day of treatment, cells were harvested ~4 hours post
725 dosage. Chronic treatments for functional experiments extended daily β-estradiol replenishments
726 for ~14 days and withdrawn 2-3 days prior to patch-clamp recordings. For RNASeq, the same
727 chronic paradigm was performed and harvested on DIV21 ~4 hours post final dosage.

728 *ii. Antisense oligonucleotide treatment*

729 A single HPLC-grade ASO was designed from Qiagen (LNA GapmeR) against the mutant (Ex
730 20/24) splice junction containing a phosphorothioate modified backbone with or without a 5'-FAM
731 label for fluorescent visualization. All experiments were performed matched with a non-targeting
732 ASO as the control group. ASOs were delivered using Lipofectamine RNAiMAX Transfection
733 Reagent (Thermo, #13778075). The Lipofectamine RNAiMAX was diluted in Opti-MEM Medium
734 (Thermo, #31985070). ASO was then diluted in Opti-MEM Medium at 1μM. The diluted ASO was
735 added in a 1:1 ratio to the diluted Lipofectamine RNAiMAX and incubated at room temperature
736 for 5 minutes. The ASO-lipid complex was added to cells, and incubated for 72 hours post-
737 transfection, until RNA harvest. ASO samples for RNA-Seq were harvested on DIV17.

738 *Molecular Biology and Imaging*

739 *i. RNA extraction and RT-qPCR*

740 For the isolation of RNA, 2D cells were lysed using TRIzol (Life Technologies #15596026) and
741 purified using the Qiagen miRNeasy Kit (Qiagen Cat# 74106) according to the manufacturer's
742 instructions. For 3D organoids, pooled (early timepoints) or single organoids were washed and
743 lysed using TRIzol, by manual homogenization with a pestle in a 1.5mL centrifuge tube. Following
744 purification, samples were normalized within each experiment (15-50ng) and subsequently used
745 for RT-qPCR assays using the *Power* SYBR Green RNA-to-Ct 1-Step Kit (Thermo REF 4389986).
746 Relative transcript abundance was determined using the ΔΔCT method and normalized to the
747 *ACTB* housekeeping gene. All primer sequences are listed below.

748 shRNA, primers and oligonucleotide probe sequences

Target	Sequences (5'-3')	Supplier
<u>RT-qPCR Primer Probes</u>		
NRXN1 (wildtype) Forward	AGAAAGATGCCAAGCACCCA	ThermoFisher
NRXN1 (wildtype) Reverse	CCCATGTCCAGGAGGAGGTA	ThermoFisher
NRXN1-20/24 (mutant) Forward	GCTACCCTGCAGCCAACC	ThermoFisher
NRXN1-20/24 (mutant) Reverse	GACCATACCCGTGGTGCTG	ThermoFisher
ACTB Forward	TGTCCCCCAACTTGAGATGT	ThermoFisher
ACTB Reverse	TGTGCACTTTTATTCAACTGGTC	ThermoFisher
MAP2 Forward	AAACTGCTCTTCCGCTCAGACACC	ThermoFisher
MAP2 Reverse	GTTCACTTGGGCAGGTCTCCACAA	ThermoFisher
NEUROD1 Forward	GGTGCCTTGCTATTCTAAGACGC	ThermoFisher
NEUROD1 Reverse	GCAAAGCGTCTGAACGAAGGAG	ThermoFisher
SLC17A7 Forward	CGCATCATGTCCACCACCAACGT	ThermoFisher
SLC17A7 Reverse	GAGTAGCCGACCACCAACAGCAG	ThermoFisher

SLC17A6 Forward	TCAACAACAGCACCATCCACCGC	ThermoFisher
SLC17A6 Reverse	GTTTCCGGGTCCCAGTTGAATTTGG	ThermoFisher
GAD65 Forward	CTATGACACTGGAGACAAGGC	ThermoFisher
GAD65 Reverse	CAAACATTTATCAACATGCGCTTC	ThermoFisher
DLX5 Forward	ACAGAGACTTCACGACTCCCAG	ThermoFisher
DLX5 Reverse	TGTGGGGCTGCTCTGGTCTA	ThermoFisher
<u>shRNA Sequences</u>		
NRXN1 wildtype mRNA (Exon 9)	ATGGAGTGGTGGCATTTAAAT	Sigma
NRXN1 mutant mRNA (Overlapping Exon 20/24)	CGCTACCCTGCAGCCAACCCA	Sigma
<u>Antisense Oligonucleotides (LNA Gapmers)</u>		
Non-targeting ASO	AACACGTCTATACGC/36-FAM/	Qiagen
NRXN1-Splice ASO	GGTTGGCTGCAGGGTA/36-FAM/	Qiagen

ii. Bright Field Imaging

For organoid perimeter analyses, brightfield microscope images of organoids were taken with a 2x objective. Image analysis was performed in ImageJ, with best fitting ovals or ellipses were selected around an organoid, and perimeter was measured.

iii. Immunostaining and imaging 2D cultures

For immunostaining of 2D monocultures, iGLUT and iGABA neurons seeded on acid-etched coverslips coated with PEI buffered with boric acid and 4x Matrigel. Samples were washed with DPBS $Ca^{2+/}Mg2^{+}$ and fixed using cold, fresh 16% paraformaldehyde (PFA, (Life Technologies, #28908)), diluted to 4% for 12 minutes at RT. Coverslips were then blocked and permeabilized with 2% donkey serum in DPBS $Ca^{2+/}Mg2^{+}$ supplemented with 0.1% Triton-X (Sigma, #93443-

760 100ML) (blocking buffer), for one hour at RT. Primary antibody solutions were prepared in
761 blocking buffer and incubated overnight at 4°C. The following day, samples were washed three
762 times with PBS, and treated with secondary antibodies diluted in blocking buffer, for 1 hour in a
763 dark chamber. Finally, samples were washed three times, and stained with DAPI for 15min at RT
764 during the final wash. Coverslips were mounted with antifade (Vectashield #H-1000-10) onto
765 glass slides and stored at 4°C until imaging using an upright Zeiss LSM 780 confocal microscope.

766 *iv. High content imaging of 2D cultures*

767 For high-content imaging, 100k cells/well were plated in an optically clear olefin bottom 96-well
768 plate (Revvity Health Sciences, #6055302). At WPI4 (iGLUT) and WPI5 (iGABA), cultures were
769 double fixed in PFA and 100% ice-cold methanol for 10min each with at least 2 washes of DPBS
770 Ca^{2+}/$Mg2^{+}$ between and after fixation steps. Fixed cultures were washed twice in PBS and
771 permeabilized and blocked two hours, followed by incubation with primary antibody solution
772 overnight at 4°C. Cultures were then washed 3 times with PBS and incubated with secondary
773 antibody solution for 1 hour at RT. Cultures were washed a further 3 timess with PBS with the
774 second wash containing 1µg/ml DAPI. Fixed cultures were then imaged on a CellInsight CX7 HCS
775 Platform with a 20x objective (0.4 NA) and neurite tracing and synaptic puncta detection
776 performed using the synaptogenesis module in the Thermo Scientific HCS Studio 4.0 Cell
777 Analysis Software to determine Syn1+ puncta density per µm of Map2+ve neurite length. 10 wells
778 were imaged per donor with 9 images acquired per well for neurite tracing analysis. Wells with
779 <10 annotated synapses, were excluded from the analysis.

Target	Antibody Dilution	Supplier/ CAT#
Primary Antibodies		
(Rabbit) vGAT	1:500	Synaptic Systems, #135-303
(Rabbit) vGLUT1	1:500	Synaptic Systems, #131-002
(Chicken) MAP2	1:1000	Abcam, #ab5392
(Mouse) Synapsin-1	1:500	Synaptic Systems, #106 011
DAPI	1:1000	Sigma, #D9542

Secondary Antibodies		
(Donkey) 488-Mouse	1:200	Jackson ImmunoResearch, # 711-545-152
(Donkey) 568-Rabbit	1:200	Abcam, #ab175700
(Donkey) 647-Chicken	1:500	Life technologies, #A10042
(Donkey) 568-Mouse	1:500	Life technologies, #A10037
(Donkey) 488-Rabbit	1:1000	Life Technologies, #A-21206

780

781 *Statistics*

782 No statistical power estimation analyses were used to predetermine sample sizes, where were
783 chosen to match previous publications[14,21] and field standards. All experimental statistics were
784 performed in Prism *v10.1.1* and R *v4.2.0.* Bioinformatic analyses were performed in R *v3.5.3* (Bulk
785 RNASeq DEG), *v4.1.2* (Bulk RNASeq GO) and *v4.1.2* (scRNAseq).

786 **Data and Code Availability**

787 All source donor hiPSCs have been deposited at the Rutgers University Cell and DNA Repository
788 (study 160; http://www.nimhstemcells.org/) and all bulk and single-cell transcriptome sequencing
789 data are being prepared for deposits to GEO. To facilitate improved reproducibility of our data
790 analyses, custom scripts has been deposited to github (https://github.com/mbfernando/NRXN1).
791 Source data will be provided with this manuscript.

792 **Acknowledgements**

793 MBF was supported by a Gilliam Fellowship from the Howard Hughes Medical Institute. This work
794 was supported by the National Institute of Mental Health grants RO1 MH121074-02 (KJB, GF and
795 PAS) and RO1 MH125579-02 (GF and KJB). DAK was supported by the National Science
796 Foundation under Grant No. DBI2146398. Any opinions, findings, and conclusions or
797 recommendations expressed in this material are those of the authors and do not necessarily
798 reflect the views of the National Science Foundation. We thank the Stem Cell Engineering Core
799 at the Icahn School of Medicine at Mount Sinai. We are grateful to the labs of Nan Yang (Ruiqi

Hu and Xiaoting Zhou) and Samuele Marro (Madel Durens) for assistance in primary glial preparations. We are especially thankful to Kayla G. Townsley and Mark G. Baxter for advice on statistical testing, and Liang Yang for critical advice on scRNASeq analyses. We acknowledge Daniel Weinberger and the Lieber Institute for Brain Development at Johns Hopkins School of Medicine, for sharing post-mortem materials. Finally, the authors thank all members of the Brennand, Slesinger and Fang labs for critical feedback and discussions throughout the course of this work.

Author Information

MBF, SK, ANM, RO, CP, AP, SG performed and analyzed experiments supervised by PAS and KJB. YZ and YF performed bioinformatic analyses supervised by GF. AT performed bioinformatic analysis of alternative splicing estimates, supervised by DAK. SW produced virus for the generation of iGABA neurons, and MD performed high-content imaging experiments. EKF processed post-mortem tissue and generated long-read data. IAP assisted in statistical analyses. MBF, GF, PAS and KJB wrote the paper with input from all authors.

Ethics declarations / Competing interest statement.

All authors have no competing interests to declare.

Figures

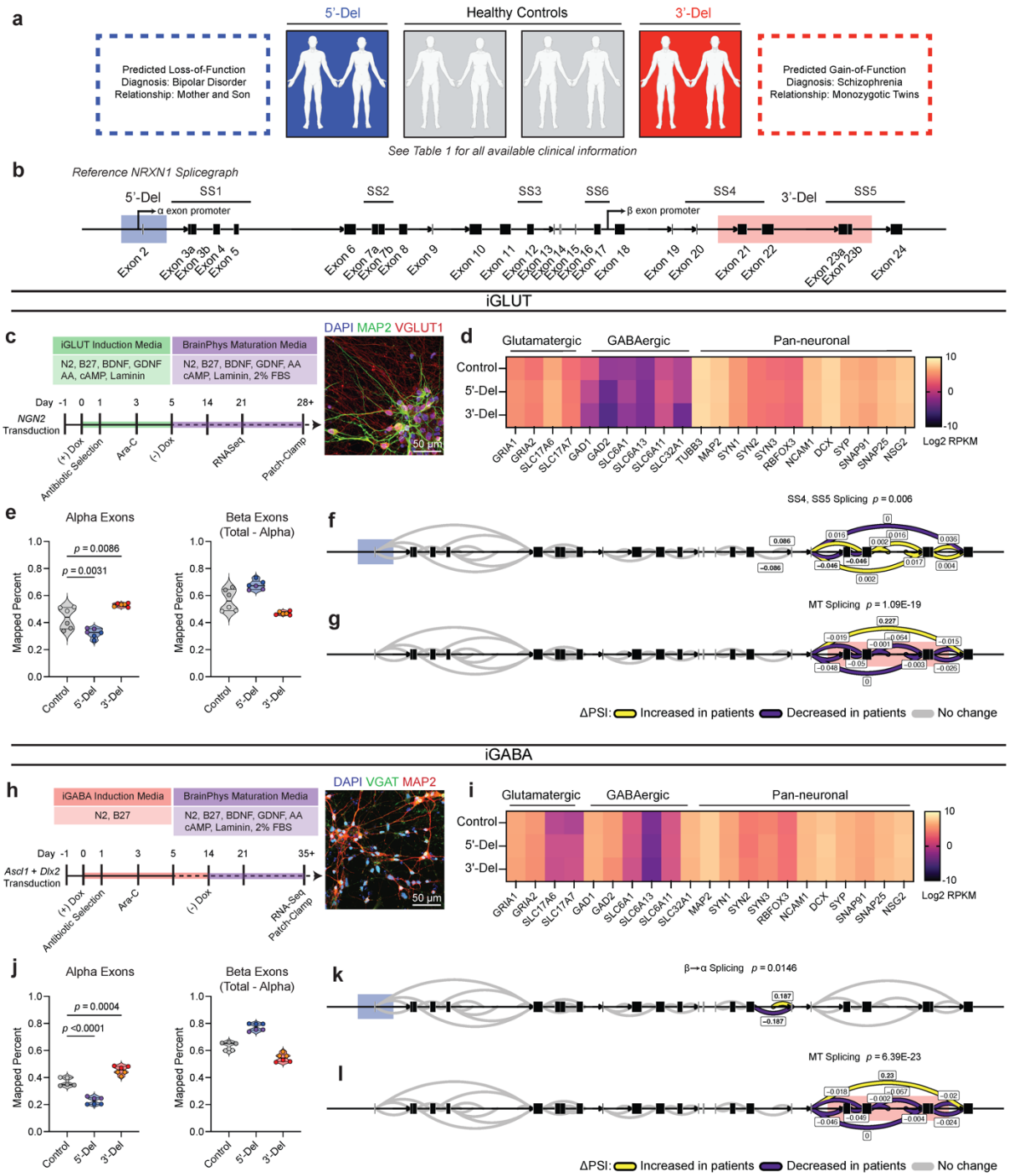

Figure 1. *Aberrant NRXN1 splicing across human iPSC derived glutamatergic (iGLUT) and GABAergic (iGABA) neurons.* (**a**) Brief description of clinical information of all hiPSC lines used in this study, and (**b**) schematic of *NRXN1* gene structure as a splicegraph, denoting splice sites (SS1-6), with red and blue shades corresponding on 3'-Del and 5'-Del genotypes, respectively.

823 Arrows indicate relative internal promoter positions. (**c, h**) Induction timeline and factors to
824 generate iGLUT and iGABA neurons, with immunostaining validation of neuronal identity (MAP2),
825 glutamate identity (vGLUT1), and GABA identity (vGAT). (**d, i**). Gene expression panel confirming
826 abundance of neuronal markers and neurotransmitter identity in iGLUT (n: Control = 6/2; 5'-Del =
827 6/2; 3'-Del = 6/2 | 1 batch) and in iGABA neurons (n: Control = 5/2; 5'-Del = 6/2; 3'-Del = 6/2 | 1
828 batch). (**e, j**) Mapped percent of alpha *NRXN1* exon reads in iGLUT, compared via a 1-way
829 ANOVA, with Dunnett's test ($F_{2, 15}$ = 25.70; 5'-Del p = 0.0031, 3'-Del p = 0.0086), and iGABA
830 neurons ($F_{2, 14}$ = 92.92; 5'-Del p < 0.001, 3'-Del p = 0.0004), with beta *NRXN1* exon reads,
831 calculated by subtracting alpha-specific reads against total reads. (**f, k**) Splicegraphs displaying
832 significant gene wide splicing clusters, compared via Dirichlet-multinomial generalized linear
833 model with Bonferroni corrections, for 5'-Del iGLUT (SS4 and SS5 cluster *p* = 0.006) and iGABA
834 neurons ($\beta \rightarrow \alpha$ cluster *p* = 0.0146), and for (**g, l**) 3'-Del iGLUT (SS4 and SS5 cluster *p* = 1.09E-
835 19) and iGABA neurons (SS4 and SS5 cluster *p* = 6.39E-23). n reported as samples/donors |
836 independent batches.

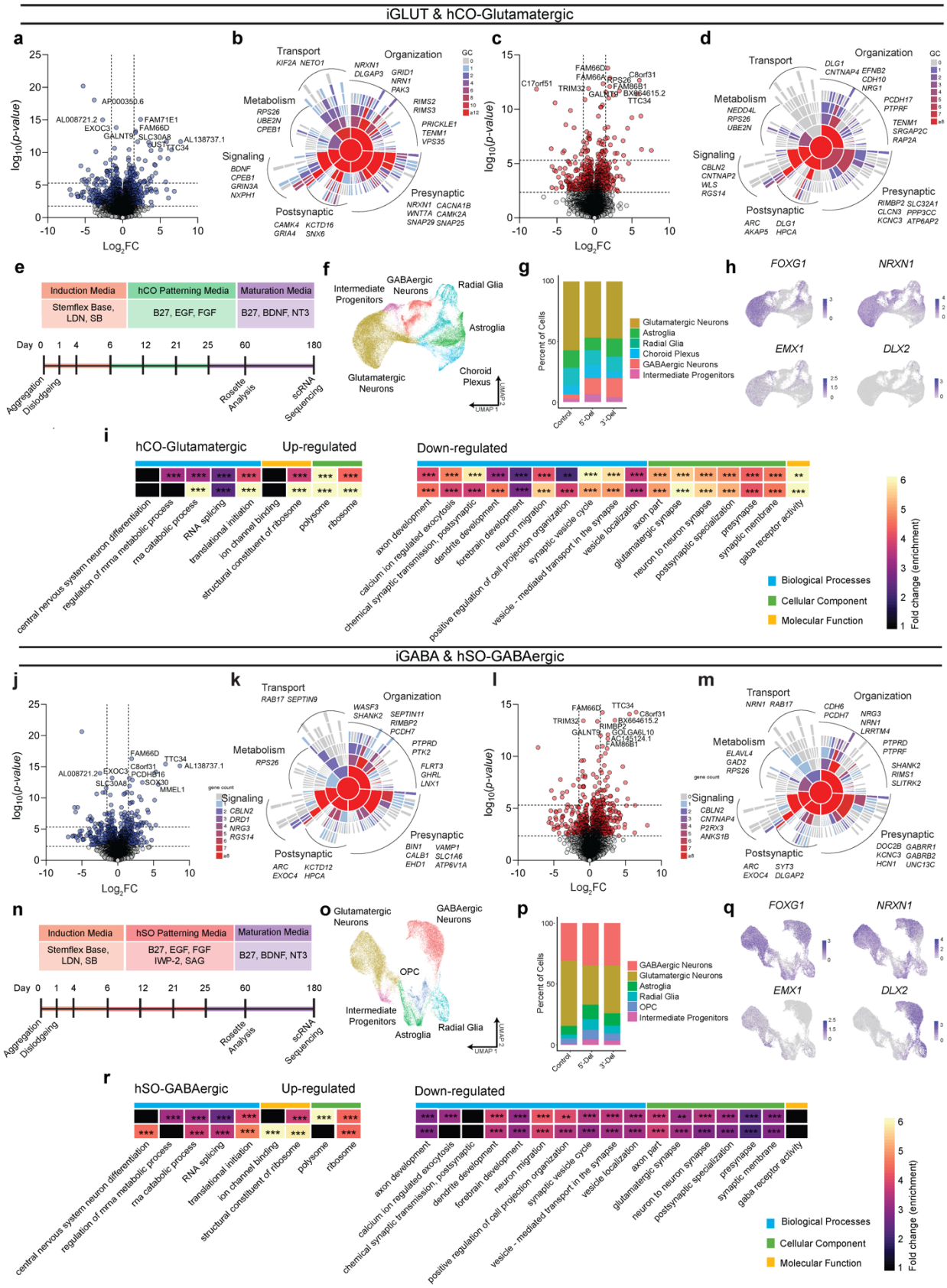
iGLUT & hCO-Glutamatergic
a
b
c
d
e
f
g
h
i
Induction Media
hCO Patterning Media
Maturation Media
Stemflex Base, LDN, SB
B27, EGF, FGF
B27, BDNF, NT3
Day 0 1 4 6 12 21 25 60 180
Aggregation
Dissociation
Rosette Analysis
scRNA Sequencing
Transport
Organization
Metabolism
Signaling
Postsynaptic
Presynaptic
Glutamatergic Neurons
Astroglia
Radial Glia
Choroid Plexus
GABAergic Neurons
Intermediate Progenitors
Control
5'-Del
3'-Del
FOXG1
NRXN1
EMX1
DLX2
hCO-Glutamatergic
Up-regulated
Down-regulated
central nervous system neuron differentiation
regulation of mrna metabolic process
rna catabolic process
RNA splicing
translational initiation
ion channel binding
structural constituent of ribosome
polysome
ribosome
axon development
calcium ion regulated exocytosis
chemical synaptic transmission, postsynaptic
dendrite development
forebrain development
neuron migration
positive regulation of cell projection organization
synaptic vesicle cycle
vesicle - mediated transport in the synapse
vesicle localization
axon part
glutamatergic synapse
neuron to neuron synapse
postsynaptic specialization
presynapse
synaptic membrane
gaba receptor activity
Biological Processes
Cellular Component
Molecular Function
Fold change (enrichment)
iGABA & hSO-GABAergic
j
k
l
m
n
o
p
q
r
Induction Media
hSO Patterning Media
Maturation Media
Stemflex Base, LDN, SB
B27, EGF, FGF IWP-2, SAG
B27, BDNF, NT3
Day 0 1 4 6 12 21 25 60 180
Aggregation
Dissociation
Rosette Analysis
scRNA Sequencing
Glutamatergic Neurons
GABAergic Neurons
OPC
Intermediate Progenitors
Radial Glia
Astroglia
hSO-GABAergic
Up-regulated
Down-regulated

838 **Figure 2**: *Transcriptomic impact of NRXN1$^{+/-}$ in induced (iGLUT/iGABA) and organoid-derived*
839 *hCO-glutamatergic and hSO-GABAergic neurons.* (**a, c**) Volcano plots of differential gene
840 expression (DE) analysis across both genotypes in iGLUT and (**j, l**) iGABA neurons. Vertical
841 dashed lines represent DE genes ±1.5 Log2FC. Horizontal dashed lines represent FDR = 0.1
842 cutoff (lower) and Bonferroni corrected cutoff (upper). (**b, d**) Sunburst plots of all FDR corrected
843 DEGs with SynGO annotated synapse function for iGLUT and (**k, m**) iGABA neurons. (**e, n**)
844 Timeline of neural organogenesis for hCO and hSOs (**f, o**), UMAPs of hCO and hSO organoid
845 samples sequenced at 6 months, annotated by cell clusters, and (**g, p**) relative proportions of cell
846 clusters across genotypes, (hCO = 47,460 cells) and (hSO = 35,563 cells). (**h, q**) validation of
847 regionalization across forebrain (*FOXG1*), dorsal (*EMX1*) and ventral (*DLX2*) regions, with
848 *NRXN1* expression across all cells. (**i, r**) Gene ontological analysis results using DEGs from
849 scRNASeq. *P < 0.05, **P < 0.01, ***P <0.001, Wilcoxon's rank sum test, FDR = 0.05. Data
850 represented as mean ± sem. n reported as samples/donors | independent batches.

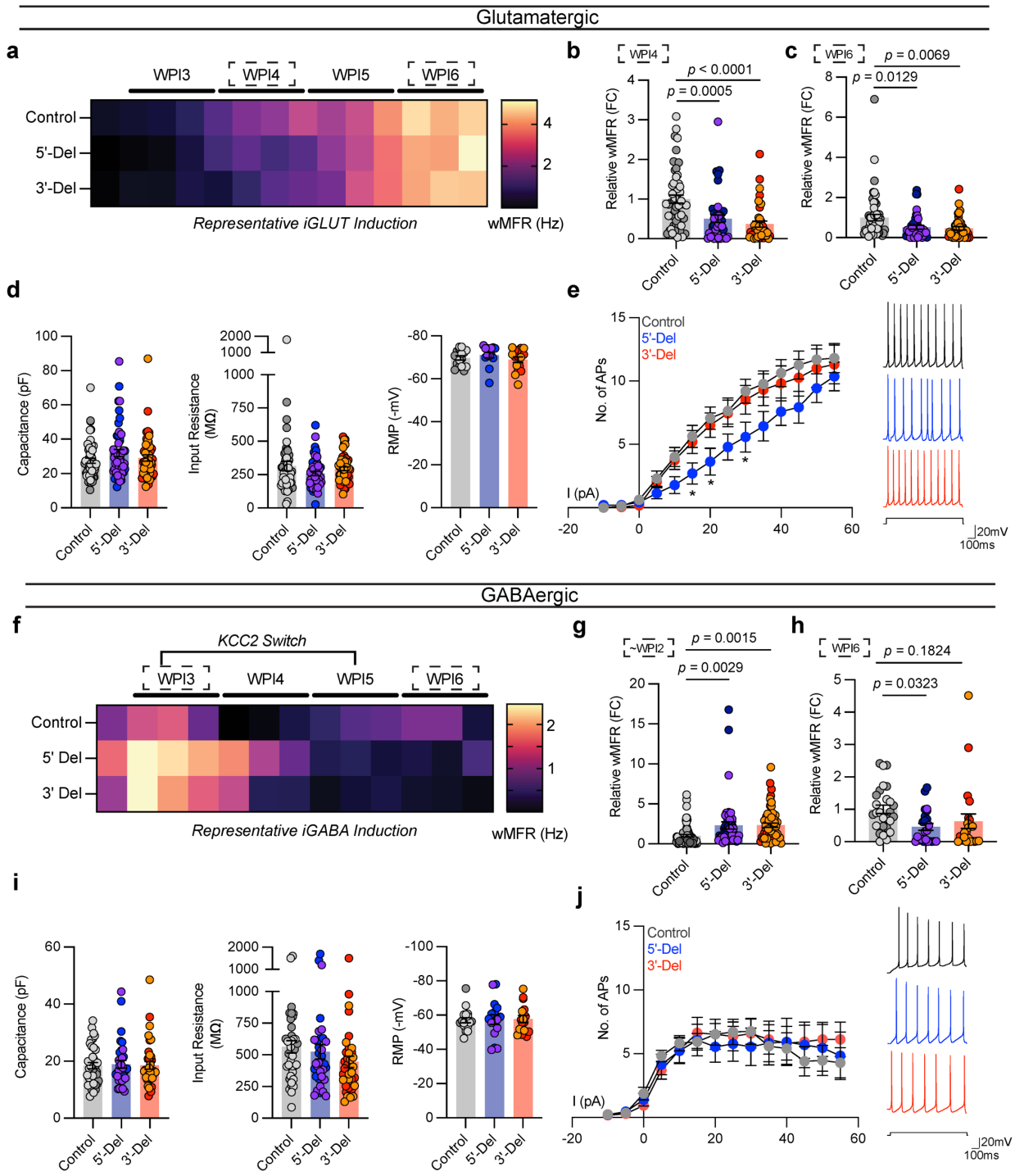
Glutamatergic
a
WPI3
WPI4
WPI5
WPI6
Control
5'-Del
3'-Del
Representative iGLUT Induction
wMFR (Hz)
b
WPI4
p < 0.0001
p = 0.0005
Relative wMFR (FC)
c
WPI6
p = 0.0069
p = 0.0129
d
Capacitance (pF)
Input Resistance (MΩ)
RMP (-mV)
e
No. of APs
I (pA)
20mV
100ms
GABAergic
f
KCC2 Switch
WPI3
WPI4
WPI5
WPI6
Control
5' Del
3' Del
Representative iGABA Induction
wMFR (Hz)
g
~WPI2
p = 0.0015
p = 0.0029
h
WPI6
p = 0.1824
p = 0.0323
i
j

852 **Figure 3.** *Spontaneous, passive, and excitable properties are minimally changed from NRXN1$^{+/-}$*
853 *induced neurons.* (**a, f**) Timelapse of multi-electrode array recordings every 2-3 days apart starting
854 near ~DIV12 for a single representative induction. Tiles represent averaged wMFR values across
855 genotypes during a single recording session. (**b**) MEA quantification of iGLUT neuronal activity,
856 compared via a 1-way ANOVA, with Dunnett's test (n: Control = 52/2; 5'-Del = 42/2; 3'-Del = 38/2
857 | 3 batches) at WPI4 ($F_{2, 129}$ = 12.77; 5'-Del p = 0.0005, 3'-Del p < 0.0001), and (**c**) WPI6 ($F_{2, 129}$ =
858 5.737; 5'-Del p = 0.0129, 3'-Del p = 0.0069). (**d**) intrinsic properties of iGLUT neurons (n: Control
859 = 51/2; 5'-Del = 51/2; 3'-Del = 48/2 | 8 batches): compared via 1-way ANOVA, with Dunnett's
860 test, Capacitance ($F_{2, 147}$ = 1.505; 5'-Del p = 0.1565, 3'-Del p = 0.7633), Input resistance ($F_{2, 147}$ =
861 1.311; 5'-Del p = 0.1949, 3'-Del p = 0.7906), and RMP (n: Control = 16/2; 5'-Del = 14/2; 3'-Del =
862 16/2 | 2 batches) compared via 1-way ANOVA, with Dunnett's test ($F_{2, 43}$ = 0.8234; 5'-Del p =
863 0.6378, 3'-Del p = 0.8468). (**e**) Input-output curves of excitable properties (n: Control = 16/2; 5'-
864 Del = 14/2; 3'-Del = 16/2 | 2 batches), with representative traces (right), compared via Step x
865 Genotype 2-way ANOVA; Dunnett's Test ($F_{26, 559}$ = 1.690, 5'-Del p < 0.01 at Step 6, 7 and 9, 3'-
866 Del p = n.s. on all steps). (**g**) MEA quantification of iGABA neuronal activity, compared via a 1-
867 way ANOVA, with Dunnett's test (n: Control = 71/2; 5'-Del = 48/2; 3'-Del = 55/2 | 5 batches) at
868 WPI2 ($F_{2, 171}$ = 7.805; 5'-Del p = 0.0029, 3'-Del p = 0.0015), and (**h**) WPI5 (n: Control = 27/4; 5'-
869 Del = 23/2; 3'-Del = 23/2 | 2 batches) compared via 1-way ANOVA, with Dunnett's test ($F_{2, 70}$ =
870 3.158; 5'-Del p = 0.0323, 3'-Del p = 0.1824). (**i**) intrinsic properties of iGABA neurons (n: Control
871 = 39/2; 5'-Del = 34/2; 3'-Del = 37/2 | 6 batches): compared via 1-way ANOVA, with Dunnett's
872 test, Capacitance ($F_{2, 107}$ = 0.04256; 5'-Del p = 0.9425, 3'-Del p = 0.9941), Input resistance (n:
873 Control = 39/2; 5'-Del = 34/2; 3'-Del = 36/2 | 6 batches, $F_{2, 106}$ = 1.451; 5'-Del p = 0.8162, 3'-Del p
874 = 0.1703) and RMP (n: Control = 18/2; 5'-Del = 16/2; 3'-Del = 16/2 | 2 batches) compared via 1-
875 way ANOVA, with Dunnett's test ($F_{2, 47}$ = 0.02842; 5'-Del p = 0.9893, 3'-Del p = 0.9601). (**j**) Input-
876 output curves of excitable properties (n: Control = 16/2; 5'-Del = 14/2; 3'-Del = 16/2 | 2 batches),
877 with representative traces (right), compared via Step x Genotype 2-way ANOVA; Dunnett's Test
878 ($F_{26, 572}$ = 0.5137, 5'-Del and 3'-Del p = n.s. on all steps). Data represented as mean ± sem. n
879 reported as samples/donors | independent batches.

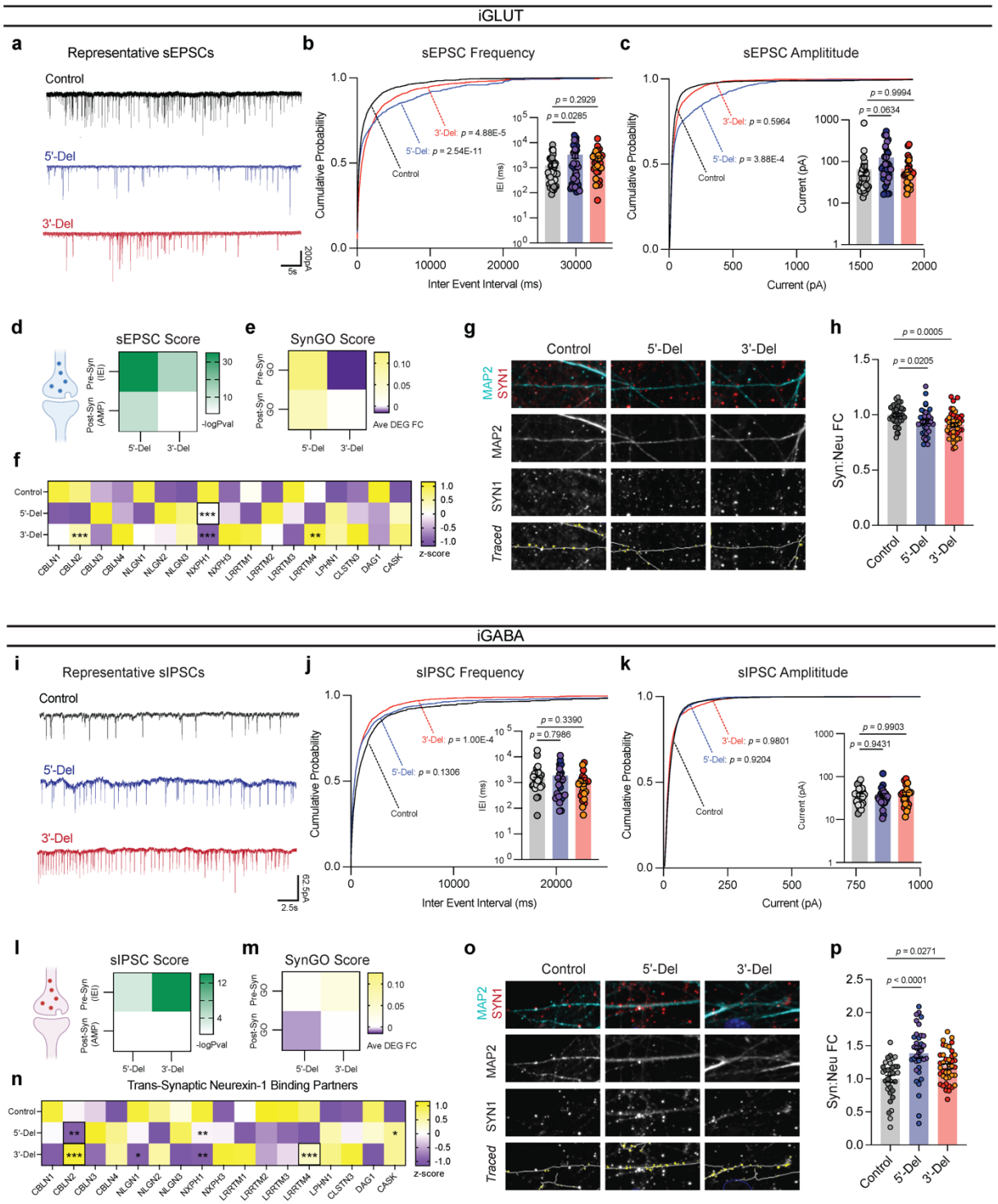
iGLUT
a
Representative sEPSCs
Control
5'-Del
3'-Del
200pA
5s
b
sEPSC Frequency
Cumulative Probability
3'-Del: p = 4.88E-5
5'-Del: p = 2.54E-11
Control
p = 0.2929
p = 0.0285
IEI (ms)
Inter Event Interval (ms)
c
sEPSC Amplitude
3'-Del: p = 0.5964
5'-Del: p = 3.88E-4
p = 0.9994
p = 0.0634
Current (pA)
d
sEPSC Score
Pre-Syn (IEI)
Post-Syn (AMP)
-logPval
e
SynGO Score
Pre-Syn GO
Post-Syn GO
Ave DEG FC
f
z-score
CBLN1 CBLN2 CBLN3 CBLN4 NLGN1 NLGN2 NLGN3 NXPH1 NXPH3 LRRTM1 LRRTM2 LRRTM3 LRRTM4 LPHN1 CLSTN3 DAG1 CASK
g
MAP2
SYN1
Traced
h
p = 0.0005
p = 0.0205
Syn:Neu FC
iGABA
i
Representative sIPSCs
62.5pA
2.5s
j
sIPSC Frequency
3'-Del: p = 1.00E-4
5'-Del: p = 0.1306
p = 0.3390
p = 0.7986
k
sIPSC Amplitude
3'-Del: p = 0.9801
5'-Del: p = 0.9204
p = 0.9903
p = 0.9431
l
sIPSC Score
m
SynGO Score
n
Trans-Synaptic Neurexin-1 Binding Partners
o
p
p = 0.0271
p < 0.0001

881 **Figure 4:** *Divergent impact on neurotransmission from NRXN1$^{+/-}$ induced neurons.* (**a**)
882 Representative traces of iGLUT sEPSCs. (**b**) Cumulative probabilities and log-scaled cell
883 averages of inter-event-internals (IEIs) across genotypes (n: Control = 39/4; 5'-Del = 33/3; 3'-Del
884 = 29/2 | 6), compared by Levene's Test with Bonferroni correction for averaged distributions (5'-
885 Del F = 46.635, df = 1, p = 2.54E-11; 3'-Del F = 17.928, df = 1, p = 4.88E-5), and 1-way ANOVA,
886 with Dunnett's test for inset ($F_{2, 98}$ = 3.117; 5'-Del p = 0.0285, 3'-Del p = 0.2929). (**c**) Cumulative
887 probabilities and log-scaled cell averages of amplitude size across genotypes, compared by
888 Levene's Test with Bonferroni correction for averaged distributions (5'-Del F = 14.15, df = 1, p =
889 3.88E-4; 3'-Del F = 1.0851, df = 1, p = 0.5964), and 1-way ANOVA, with Dunnett's test for inset
890 ($F_{2, 98}$ = 2.839; 5'-Del p = 0.0634, 3'-Del p = 0.9994). (**d**) Transformed p-values of Levene's Test
891 and (**e**) SynGO gene-set averaged log_2FC values across pre- or post- synaptic genes. (**f**) Gene
892 expression panel (z-scores), of canonical *NRXN1* binding partners in iGLUT neurons, boxes
893 indicate reaching genome wide significance. (**g**) Representative images of iGLUT synaptic puncta
894 traced (SYN1) onto dendrites (MAP2), and (**h**) normalized fold change of SYN1 puncta to length
895 of MAP2 ratio (Syn:Neu), (n: Control = 40/2; 5'-Del: 39/2; 3'-Del: 40/2), compared via 1-way
896 ANOVA, with Dunnett's test ($F_{2, 116}$ = 7.538, 5'-Del p = 0.0205, 3'-Del p = 0.0005). (**i**)
897 Representative traces of iGABA sIPSCs. (**j**) Cumulative probabilities and log-scaled cell averages
898 of inter-event-internals (IEIs) across genotypes (n: Control = 26/2; 5'-Del = 25/3; 3'-Del = 22/2 |
899 4), compared by Levene's Test with Bonferroni correction for averaged distributions (5'-Del F =
900 3.4002, df = 1, p = 0.1306; 3'-Del F = 16.501, df = 1, p = 1.00E-04), and 1-way ANOVA, with
901 Dunnett's test for inset ($F_{2, 70}$ = 0.8296; 5'-Del p = 0.7986, 3'-Del p = 0.339). (**k**) Cumulative
902 probabilities and log-scaled cell averages of amplitude size across genotypes, compared by
903 Levene's Test for averaged distributions (5'-Del F = 0.1, df = 1, p = 0.9204; 3'-Del F = 0.0006, df
904 = 1, p = 0.9801), and 1-way ANOVA, with Dunnett's test for inset ($F_{2, 70}$ = 0.08143; 5'-Del p =
905 0.9431, 3'-Del p = 0.9904). (**l**) Transformed p-values of Levene's Test and (**m**) SynGO gene-set
906 averaged log_2FC values across pre- or post- synaptic genes. (**n**) Gene expression panel (z-
907 scores), of canonical *NRXN1* binding partners in iGABA neurons, boxes indicate reaching
908 genome wide significance. (**o**) Representative images of iGABA synaptic puncta traced (SYN1)
909 onto dendrites (MAP2), and (**p**) normalized fold change of SYN1 puncta to length of MAP2 ratio
910 (Syn:Neu), (n: Control = 33/2; 5'-Del: 36/2; 3'-Del: 40/2), compared via 1-way ANOVA, with
911 Dunnett's test ($F_{2, 101}$ = 12.59, 5'-Del p < 0.0001, 3'-Del p = 0.0271). *p < 0.05, **p < 0.01, ***p
912 <0.001, Wilcoxon's rank sum test, FDR = 0.05. Data represented as mean ± sem. n reported as
913 samples/donors | independent batches.

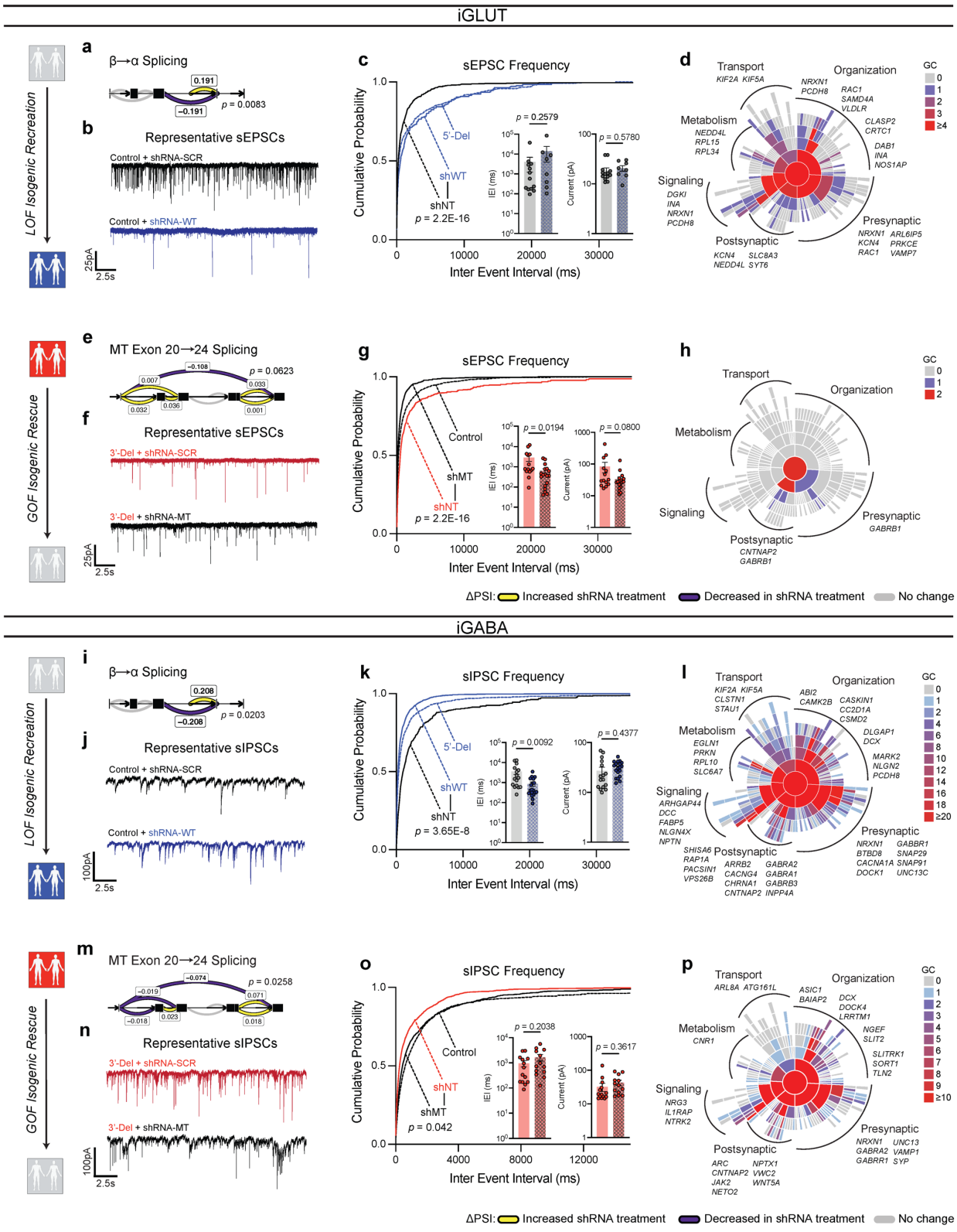
iGLUT
LOF Isogenic Recreation
GOF Isogenic Rescue
a
β→α Splicing
0.191
−0.191
p = 0.0083
b
Representative sEPSCs
Control + shRNA-SCR
Control + shRNA-WT
25pA
2.5s
c
sEPSC Frequency
Cumulative Probability
5'-Del
shWT
shNT
p = 2.2E-16
p = 0.2579
p = 0.5780
IEI (ms)
Current (pA)
Inter Event Interval (ms)
d
Transport
Organization
Metabolism
Signaling
Presynaptic
Postsynaptic
GC
e
MT Exon 20→24 Splicing
−0.108
p = 0.0623
0.007
0.033
0.032
0.036
0.001
f
Representative sEPSCs
3'-Del + shRNA-SCR
3'-Del + shRNA-MT
g
sEPSC Frequency
Control
shMT
shNT
p = 2.2E-16
p = 0.0194
p = 0.0800
h
ΔPSI: Increased shRNA treatment
Decreased in shRNA treatment
No change
iGABA
i
β→α Splicing
0.208
−0.208
p = 0.0203
j
Representative sIPSCs
Control + shRNA-SCR
Control + shRNA-WT
100pA
k
sIPSC Frequency
5'-Del
shWT
shNT
p = 3.65E-8
p = 0.0092
p = 0.4377
l
m
MT Exon 20→24 Splicing
−0.074
p = 0.0258
−0.019
0.071
−0.018
0.023
0.018
n
Representative sIPSCs
3'-Del + shRNA-SCR
3'-Del + shRNA-MT
o
sIPSC Frequency
Control
shNT
shMT
p = 0.042
p = 0.2038
p = 0.3617
p

Figure 5: *Isogenic recapitulation and rescue of neurotransmission phenotypes.* (**a**) Differential splicing of β→α cluster in shWT, compared via Dirichlet-multinomial generalized linear model (*p* = 0.0083) in iGLUT neurons. (**b**) Representative traces of iGLUT WT knockdown effects, with (**c**) cumulative probabilities of sEPSC IEI distributions, with insets of cell-averaged IEI and amplitude measures (n: shNT = 12/1; shWT = 7/1 | 2 batches). Curves were compared via a Levene's test (F = 70.78, df =1, *p* < 2.2E-16), and insets were compared via a Student's t-test (IEI t=1.166, df=19, *p* = 0.2579; AMP t=0.5661, df=19, *p* = 0.578). (**d**) SynGO (biological process) sunburst plots showing enrichment of DEGs associated with synaptic function for iGLUT WT-KD compared to a brain expressed background via Fisher's exact test (1.274161-fold, *p* = 0.1049). (**e**) Splicing of MT exon 20→24 cluster in shMT, compared via Dirichlet-multinomial generalized linear model (*p* = 0.0623). (**f**) Representative traces of iGLUT MT knockdown effects, with (**g**) cumulative probabilities of sEPSC IEI distributions, with insets of cell-averaged IEI and amplitude measures (n:shNT = 14/1; shMT = 18/1 | 2 batches). Curves were compared via a Levene's test (F = 230.6; df = 1, *p* < 2.2E-16), and insets were compared via a Student's t-test (IEI t=2.471, df=30, *p* = 0.0194; AMP t=1.812, df=30, *p* = 0.08). (**h**) SynGO (biological process) sunburst plots showing enrichment of DEGs associated with synaptic function for iGLUT MT-KD compared to a brain expressed background via Fisher's exact test (1.214533-fold, *p* = 0.4541). (**i**) Differential splicing of β→α cluster in shWT, compared via Dirichlet-multinomial generalized linear model (*p* = 0.0203) in iGABA neurons. (**j**) Representative traces of iGABA WT knockdown effects, with (**k**) cumulative probabilities of sIPSC IEI distributions, with insets of cell-averaged, IEI and amplitude measures (shNT = 16/3; shWT = 19/3 | 2 batches). Curves were compared via a Levene's test (F = 30.879, df =1, *p* < 3.66E-08), and insets were compared via a Student's t-test (IEI t=2.768, df=33, *p* = 0.0092; AMP t=0.7856, df=33, *p* = 0.4377). (**l**) SynGO (biological process) sunburst plots for iGABA WT-KD compared to a brain expressed background via Fisher's exact test (1.234861-fold, *p* = 1.307E-6). (**m**) Splicing of MT exon 20→24 cluster in shMT, compared via Dirichlet-multinomial generalized linear model (*p* = 0.0258) in iGABA neurons. (**n**) Representative traces of iGABA MT knockdown effects, with (**o**) cumulative probabilities of sIPSC IEI distributions, with insets of cell-averaged, IEI and amplitude measures (shNT = 16/1; shMT = 19/1 | 2 batches). Curves were compared via a Levene's test (F = 4.1324; df = 1, *p* < 0.04226), and insets were compared via a Student's t-test (IEI t=1.305, df=25, *p* = 0.2038; AMP t=0.9292, df=25, *p* = 0.3617). (**p**) SynGO (biological process) sunburst plots for iGABA WT-KD compared to a brain expressed background via Fisher's exact test (1.347225-fold, *p* = 2.694E-4). Data represented as mean ± sem. n reported as samples/donors | independent batches.

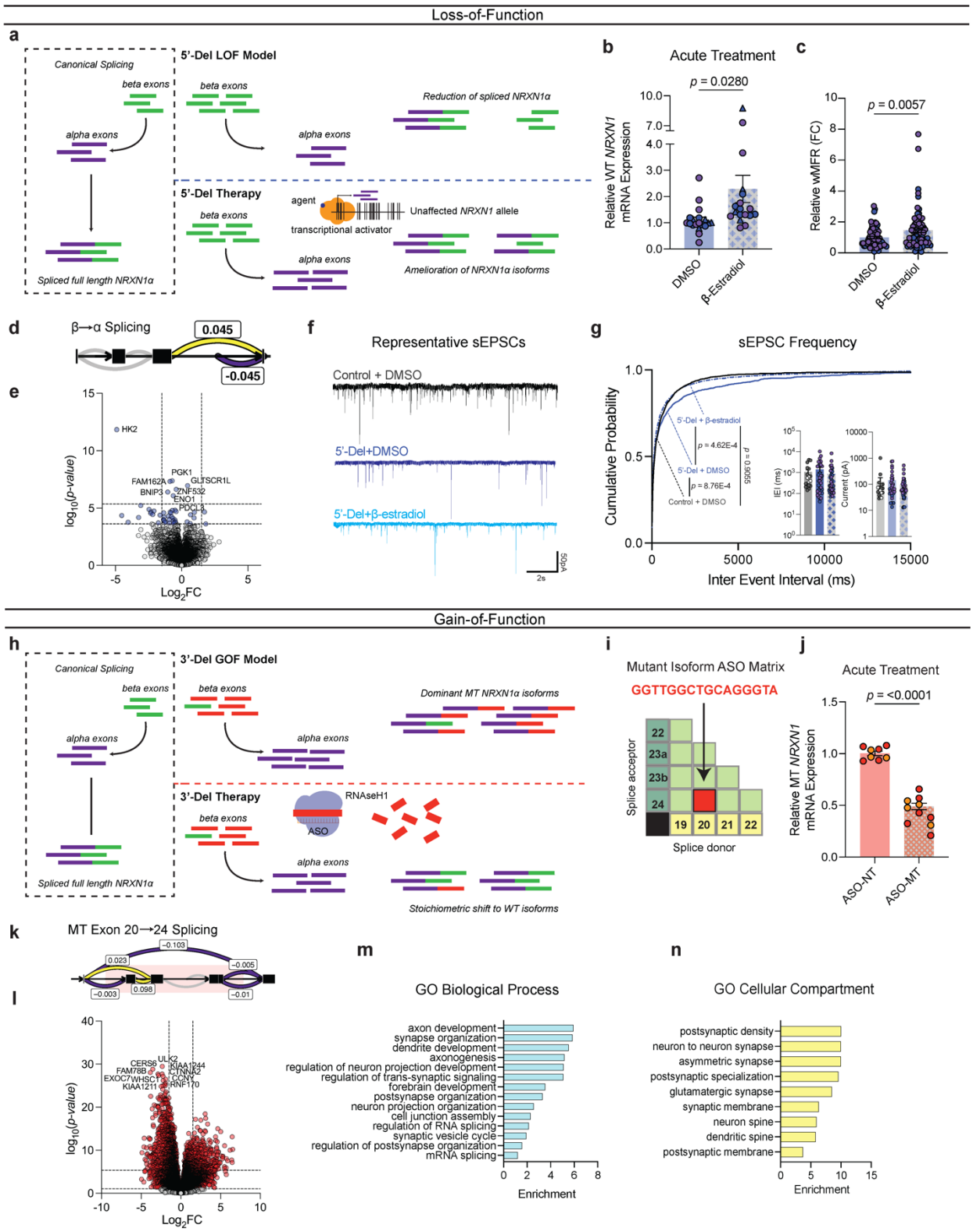

Loss-of-Function
a
Canonical Splicing
beta exons
alpha exons
Spliced full length NRXN1α
5'-Del LOF Model
beta exons
alpha exons
Reduction of spliced NRXN1α
5'-Del Therapy
beta exons
agent
transcriptional activator
Unaffected NRXN1 allele
alpha exons
Amelioration of NRXN1α isoforms
b
Acute Treatment
p = 0.0280
Relative WT NRXN1 mRNA Expression
DMSO
β-Estradiol
c
p = 0.0057
Relative wMFR (FC)
DMSO
β-Estradiol
d
β→α Splicing
0.045
-0.045
e
HK2
PGK1
FAM162A
GLTSCR1L
BNIP3
ZNF532
ENO1
PDCL3
log10(p-value)
Log2FC
f
Representative sEPSCs
Control + DMSO
5'-Del+DMSO
5'-Del+β-estradiol
50pA
2s
g
sEPSC Frequency
Cumulative Probability
5'-Del + β-estradiol
p = 4.62E-4
5'-Del + DMSO
p = 8.76E-4
Control + DMSO
p = 0.9055
IEI (ms)
Current (pA)
Inter Event Interval (ms)
Gain-of-Function
h
Canonical Splicing
beta exons
alpha exons
Spliced full length NRXN1α
3'-Del GOF Model
beta exons
alpha exons
Dominant MT NRXN1α isoforms
3'-Del Therapy
beta exons
RNAseH1
ASO
alpha exons
Stoichiometric shift to WT isoforms
i
Mutant Isoform ASO Matrix
GGTTGGCTGCAGGGTA
Splice acceptor
Splice donor
22
23a
23b
24
19
20
21
22
j
Acute Treatment
p = <0.0001
Relative MT NRXN1 mRNA Expression
ASO-NT
ASO-MT
k
MT Exon 20→24 Splicing
0.023
-0.103
-0.005
-0.003
0.098
-0.01
l
CERS6
ULK2
FAM78B
KIAA1244
EXOC7
WHSC1
CTNNA2
KIAA1211
CCNY
RNF170
log10(p-value)
Log2FC
m
GO Biological Process
axon development
synapse organization
dendrite development
axonogenesis
regulation of neuron projection development
regulation of trans-synaptic signaling
forebrain development
postsynapse organization
neuron projection organization
cell junction assembly
regulation of RNA splicing
synaptic vesicle cycle
regulation of postsynapse organization
mRNA splicing
Enrichment
n
GO Cellular Compartment
postsynaptic density
neuron to neuron synapse
asymmetric synapse
postsynaptic specialization
glutamatergic synapse
synaptic membrane
neuron spine
dendritic spine
postsynaptic membrane
Enrichment

949 **Figure 6:** *Precise therapeutic targeting of stratified GOF- and LOF-NRXN1$^{+/-}$ in iGLUT neurons.*
950 (**a**) Model and proposed mechanism of rescue for LOF patients ameliorating loss of wildtype
951 isoforms. (**b**) RT-qPCR of WT *NRXN1* gene expression in 5-Del patients, post-acute treatment
952 (3-5 days) (n: DMSO = 19/2; β-estradiol = 18/2 | 3 batches) compared via Student's t-test
953 t=2.293, df=35, p = 0.028. (**c**) Quantification of iGLUT neuronal activity at WPI3 across vehicle
954 and treatment (n: DMSO = 72/3; β-estradiol = 74/3 | 3 batches) compared via Student's t-test
955 (t=2.804, df=144, p = 0.0057). (**d**) Splicing of β→α cluster and (**e**) volcano plot of DEGs in β-
956 estradiol treated 5'-Del iGLUT neurons, compared to vehicle treated 5'-Del iGLUT neurons. (**f**)
957 Representative patch-clamp traces and (**h**) cumulative probabilities of sEPSC IEI distributions,
958 with insets of cell-averaged, IEI and amplitude measures (n: Control + DMSO = 18/1; 5'-Del +
959 DMSO = 33/2 5'-Del + β-estradiol = 35/2). Curves were compared via Levene's test with
960 Bonferroni corrections (Control + DMSO v. 5'-Del + DMSO F = 13.151; df = 1, p = 8.763E-4; 5'-
961 Del + DMSO v 5'-Del + β-estradiol F = 14.359; df = 1, p = 4.62E-04; Control + DMSO v 5'-Del +
962 β-estradiol, F = 0.0141; df = 1, p = 0.955). Insets were compared via Student's t-test (IEI t=1.161,
963 df=66, p = 0.2499). (**h**) Model and proposed mechanism of rescue for GOF patients expressing
964 mutant isoforms. (**i**) Schematic of a *NRXN1* ASO matrix, with the selective sequence targeting
965 20/24 splice junction. (**j**) RT-qPCR of MT *NRXN1* gene expression in 3'-Del patients' post-acute
966 treatment for 72hrs (ASO-NT = 8/2; ASO-MT = 10/2 | batches),compared via Student's t-test
967 t=12.91, df=16 p < 0.0001. (**k**) Splicing of MT Exon 20→24 cluster and (**l**) volcano plot of DEGs
968 in ASO-MT treated 3'-Del iGLUT neurons, compared to ASO-NT treated 3'-Del iGLUT
969 neurons.(**m**) Biological process and (**n**) cellular compartment GO terms demonstrating
970 enrichment ($-\log_{10}$[adj p value]) of selected synapse related pathways. Data represented as mean
971 ± sem. n reported as samples/donors | independent batches.

972

Extended Data Figures

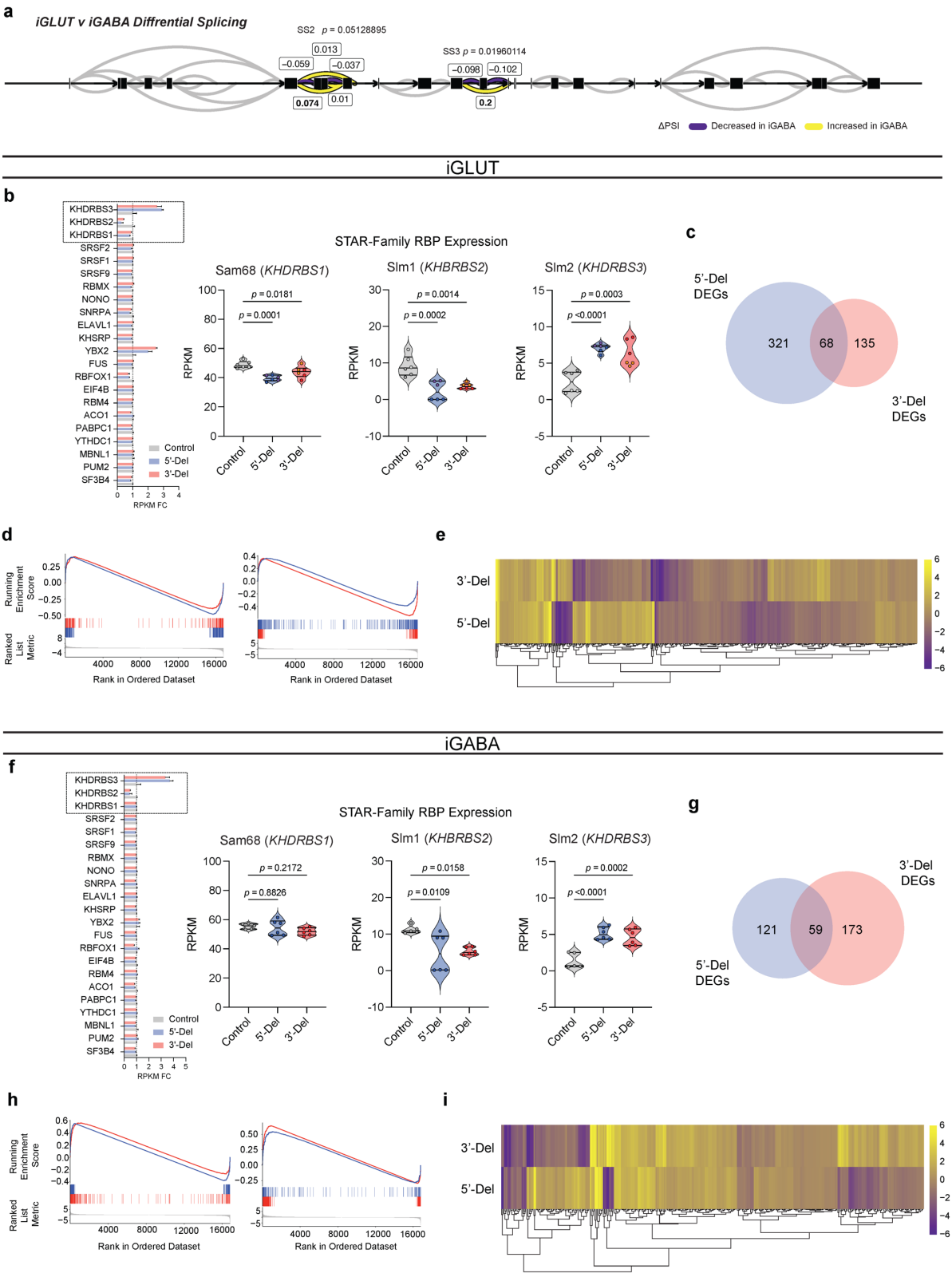

974

975 **Extended Data Figure 1:** (**a**) Splicegraph displaying significant gene wide splicing clusters at
976 *NRXN1* SS3 (p = 0.0196), compared via Dirichlet-multinomial generalized linear model with
977 Bonferroni corrections. (**b, f**) Gene expression fold-change of select *NRXN1* predicted RNA-
978 binding proteins (RBP) across patients and control iGLUT and iGABA neurons, with statistical
979 comparisons for STAR-Family RBPs. (**c, g**) Overlap of DEGs and (**d,h)** gene set enrichment
980 analysis (GSEA) between genotypes. (**e,i**) Distinct gene expression patterns by hierarchal
981 clustering of all patient specific DEGs. Sample information correspond to Fig. 1

a

	iGLUT 5'-Del		iGLUT 3'-Del		iGABA 5'-Del		iGABA 3'-Del	
	Overlapped DEGs with risk genes	Overlapped DEGs with risk genes & in SIGNOR database	Overlapped DEGs with risk genes	Overlapped DEGs with risk genes & in SIGNOR database	Overlapped DEGs with risk genes	Overlapped DEGs with risk genes & in SIGNOR database	Overlapped DEGs with risk genes	Overlapped DEGs with risk genes & in SIGNOR database
ASD	11	**7**	4	**0**	3	**1**	6	**2**
BP	16	**9**	3	**1**	2	**1**	5	**1**
SCZ	26	**14**	10	**1**	9	**3**	14	**3**
Total	37	**22**	12	**2**	9	**3**	18	**4**

iGLUT

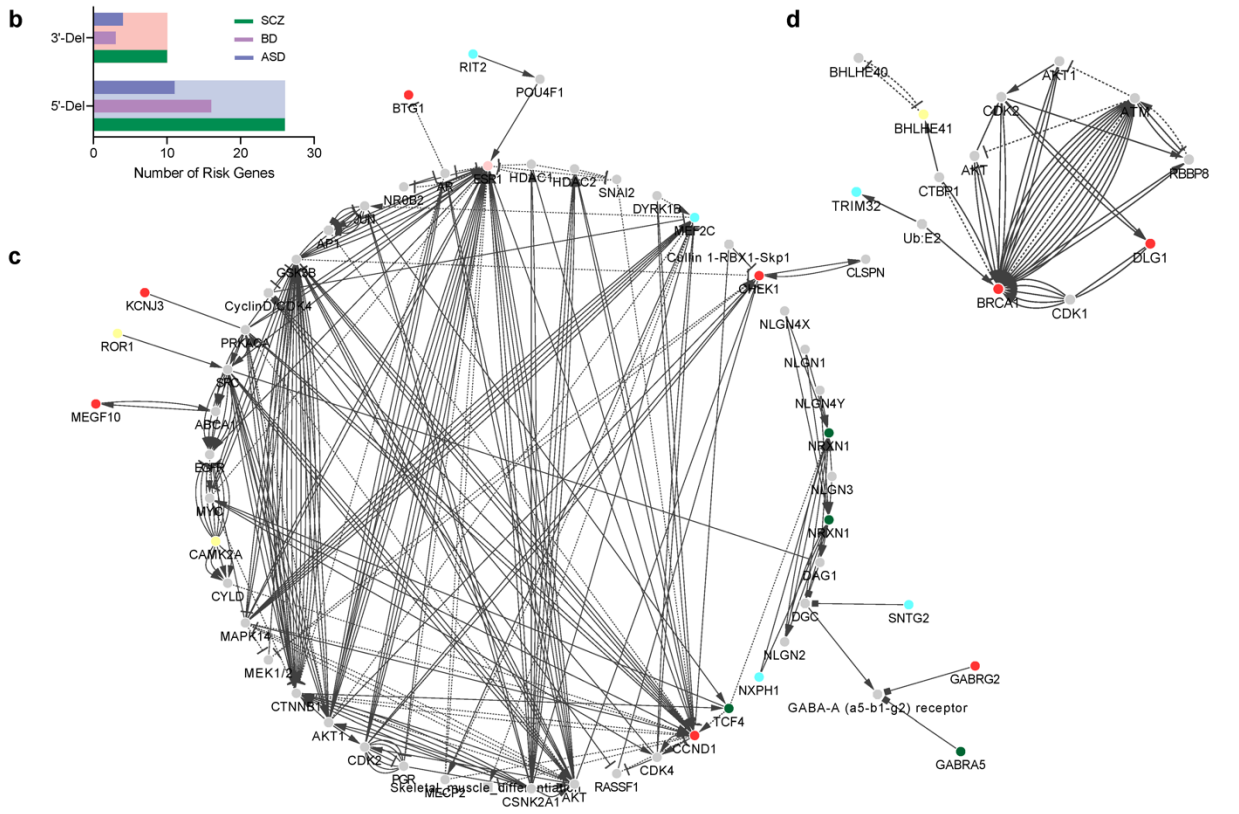

iGABA

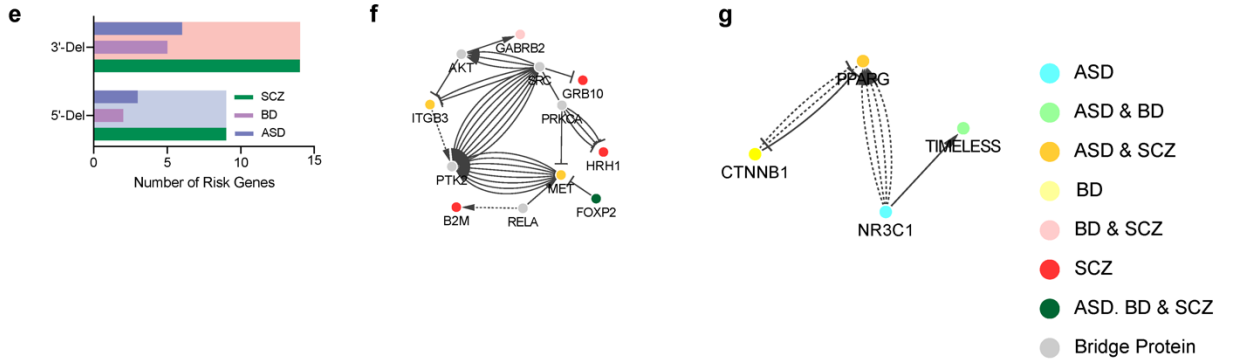

982

983

984 **Extended Data Figure 2:** *Extended transcriptomics analysis on disease risk associated genes.*
985 (a) Summary table of overlapping DEGs with risk enrichments across publicly curated datasets
986 for autism (ASD), bipolar disorder (BD) and schizophrenia. (**b, e**) Enrichment of genes across
987 neuropsychiatric disorders for iGLUT and iGABA neurons. (**c**) Interaction maps of risk genes for
988 5'-Del iGLUT, (**d**) 3'-Del iGLUT, (**f**) 5'-Del iGABA and (**g**) 5'-iGABA. Sample information
989 correspond to Fig. 1

990

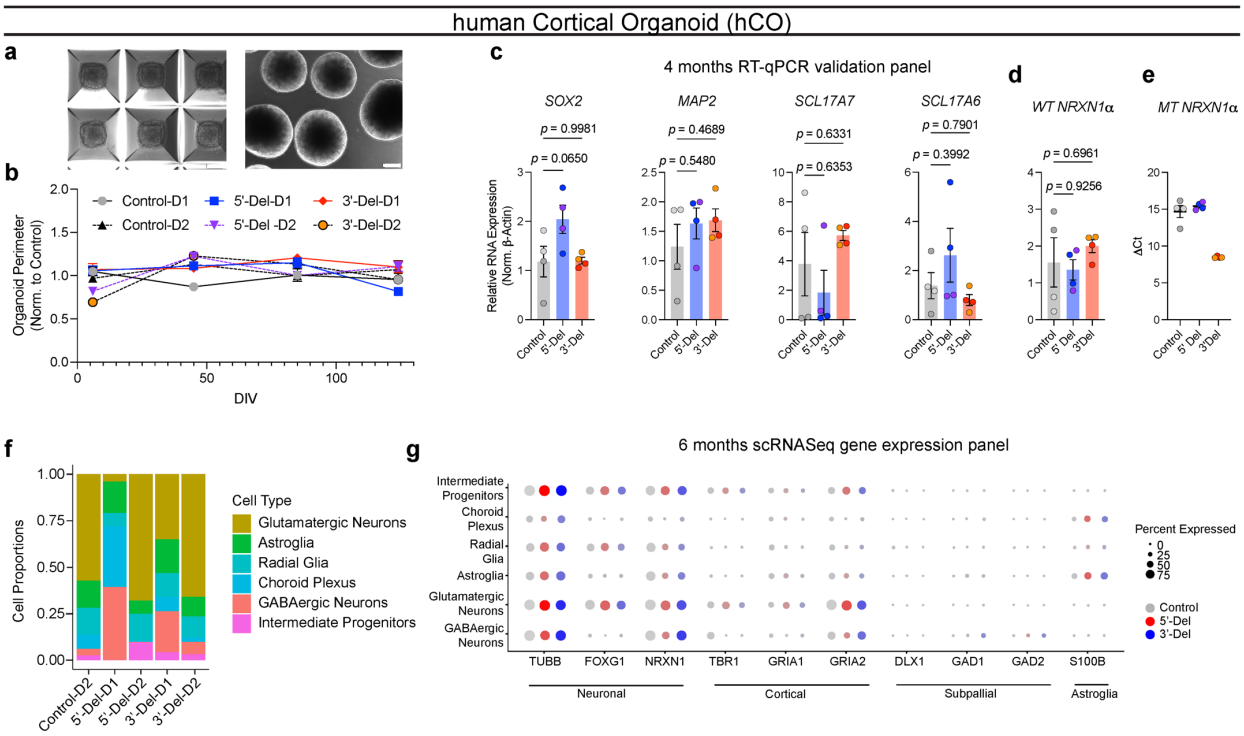
human Cortical Organoid (hCO)
a
b
Control-D1
5'-Del-D1
3'-Del-D1
Control-D2
5'-Del -D2
3'-Del-D2
Organoid Perimeter (Norm. to Control)
DIV
c
4 months RT-qPCR validation panel
SOX2
MAP2
SCL17A7
SCL17A6
Relative RNA Expression (Norm. β-Actin)
Control
5'-Del
3'-Del
d
WT NRXN1α
e
MT NRXN1α
ΔCt
f
Cell Proportions
Control-D2
5'-Del-D1
5'-Del-D2
3'-Del-D1
3'-Del-D2
Cell Type
Glutamatergic Neurons
Astroglia
Radial Glia
Choroid Plexus
GABAergic Neurons
Intermediate Progenitors
g
6 months scRNASeq gene expression panel
Intermediate Progenitors
Choroid Plexus
Radial Glia
Astroglia
Glutamatergic Neurons
GABAergic Neurons
TUBB
FOXG1
NRXN1
TBR1
GRIA1
GRIA2
DLX1
GAD1
GAD2
S100B
Neuronal
Cortical
Subpallial
Astroglia
Percent Expressed
Control
5'-Del
3'-Del

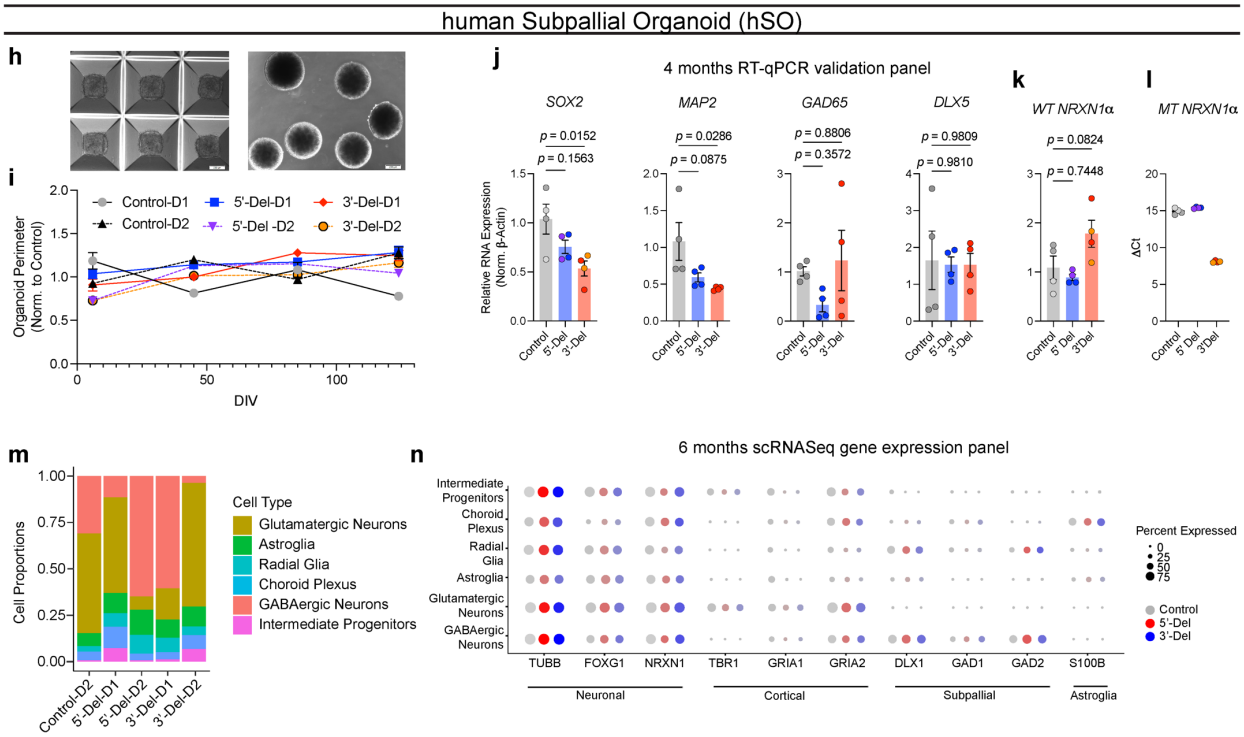
human Subpallial Organoid (hSO)
h
i
Control-D1
5'-Del-D1
3'-Del-D1
Control-D2
5'-Del -D2
3'-Del-D2
Organoid Perimeter (Norm. to Control)
DIV
j
4 months RT-qPCR validation panel
SOX2
MAP2
GAD65
DLX5
Relative RNA Expression (Norm. β-Actin)
Control
5'-Del
3'-Del
k
WT NRXN1α
l
MT NRXN1α
ΔCt
m
Cell Proportions
Control-D2
5'-Del-D1
5'-Del-D2
3'-Del-D1
3'-Del-D2
Cell Type
Glutamatergic Neurons
Astroglia
Radial Glia
Choroid Plexus
GABAergic Neurons
Intermediate Progenitors
n
6 months scRNASeq gene expression panel
Intermediate Progenitors
Choroid Plexus
Radial Glia
Astroglia
Glutamatergic Neurons
GABAergic Neurons
TUBB
FOXG1
NRXN1
TBR1
GRIA1
GRIA2
DLX1
GAD1
GAD2
S100B
Neuronal
Cortical
Subpallial
Astroglia
Percent Expressed
Control
5'-Del
3'-Del

992 **Extended Data Figure 3:** *Extended data on human organoid generation and characterization.*
993 (**a,h**) Representative images of hiPSC aggregation and immature spheroids post dislodging. (**b,i**)
994 Normalized organoid perimeters over time (compared to averaged control), hCO (n = 6 donors |
995 2 batches | 72-161 organoids) and hSO (n = 6 donors | 2 batches | 46-134 organoids). (**c, j**) RT-
996 qPCR results from 4-month organoids of genes for pluripotency, neuronal, and cell-type specific
997 markers. (d-e, k-l) RT-qPCR results of *NRXN1* WT and MT expression hCO (n = 6 donors | 1
998 representative batch | 12 samples) and hSO (n = 6 donors | 1 representative batch | 12 samples).
999 Statistical tests used were 1-way ANOVAs with Dunnett's test. (f, m) relative proportions of cell
1000 clusters across individual donors, (hCO = 47,460 cells) and (hSO = 35,563 cells). (**g, n**)
1001 Comprehensive gene expression panel across sub-clusters of hCO and hSO samples across
1002 neuronal, cortical, subpallial and astroglia markers. Data corresponds to Fig 2.

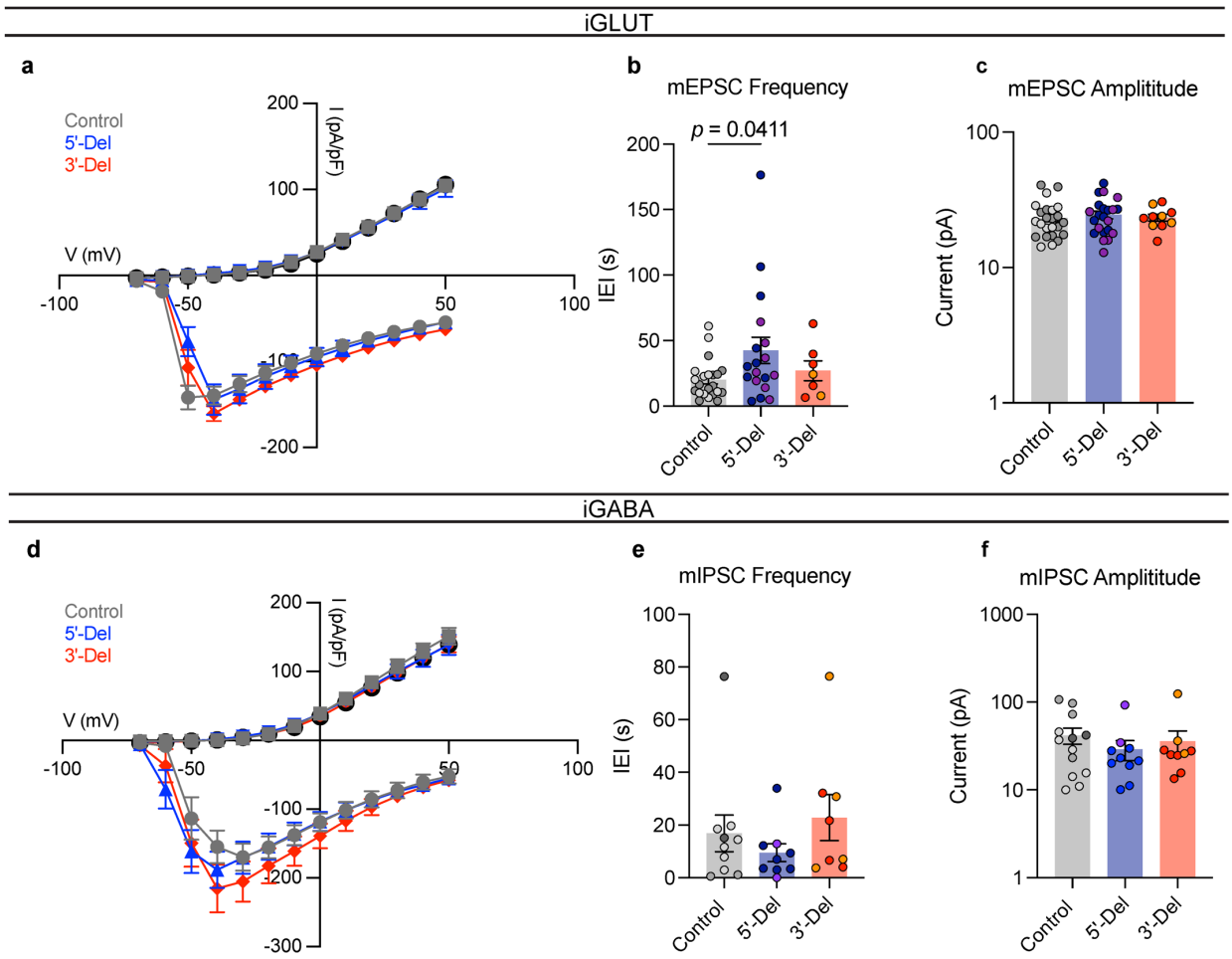

1003
1004 **Extended Data Figure 4:** *Extended data on electrophysiological properties of 5'-Del and 3'-Del*
1005 *neurons.* (**a**) Voltage-gated potassium and channel kinetics across genotypes for iGLUT neurons
1006 (n = 6 donors | 2 inductions | 45 neurons). (**b**) Comparative mEPSC kinetics of IEI and (**c**)

amplitude size from iGLUT neurons (n= 6 donors | 4 inductions | 47 neurons), compared via a 1-way ANOVA with Dunnett's test. (**d**) Voltage-gated potassium and channel kinetics across genotypes for iGABA neurons (n = 6 donors | 2 inductions | 34 neurons). (**e**) Comparative mIPSC kinetics of (a) IEI and (**f**) amplitude size from iGABA neurons (n= 6 donors | 3 inductions | 27 neurons), compared via a 1-way ANOVA with Dunnett's test. See Supplementary Table 5 for all summary statistics.

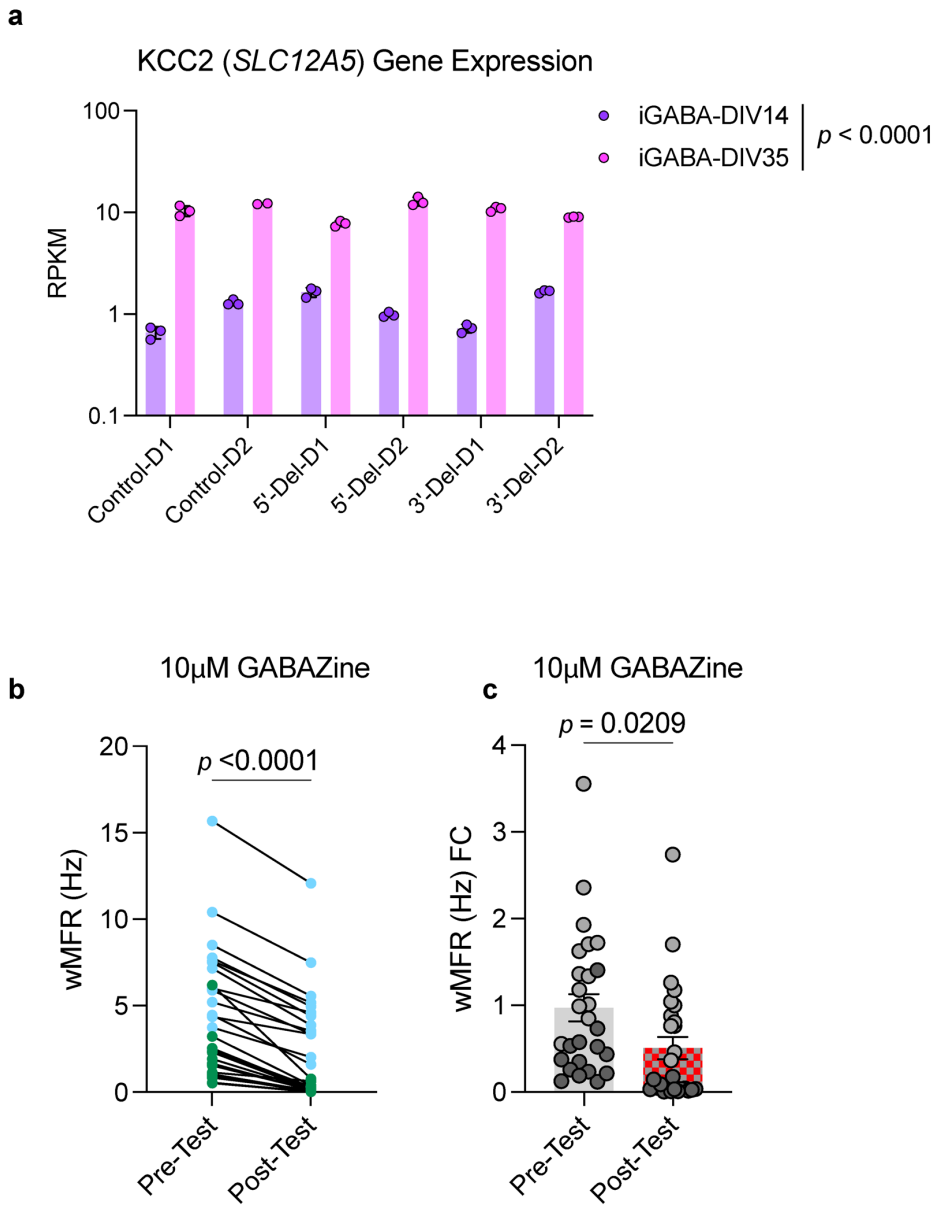

Extended Data Figure 5: *Extended KCC2 related data from immature GABA neurons.* (a) Transcriptomic comparison of *SLC12A5* expression across DIV14 and DIV35 RNASeq

timepoints. (b,c) MEA tests from pre- and post- treatment of 10uM GABAzine. (n = 2 donors | 1 representative induction | 28 MEA wells) Statistical tests are paired student's t-test for time-linked comparison and unpaired student's t-test for pre/post activity foldchange.

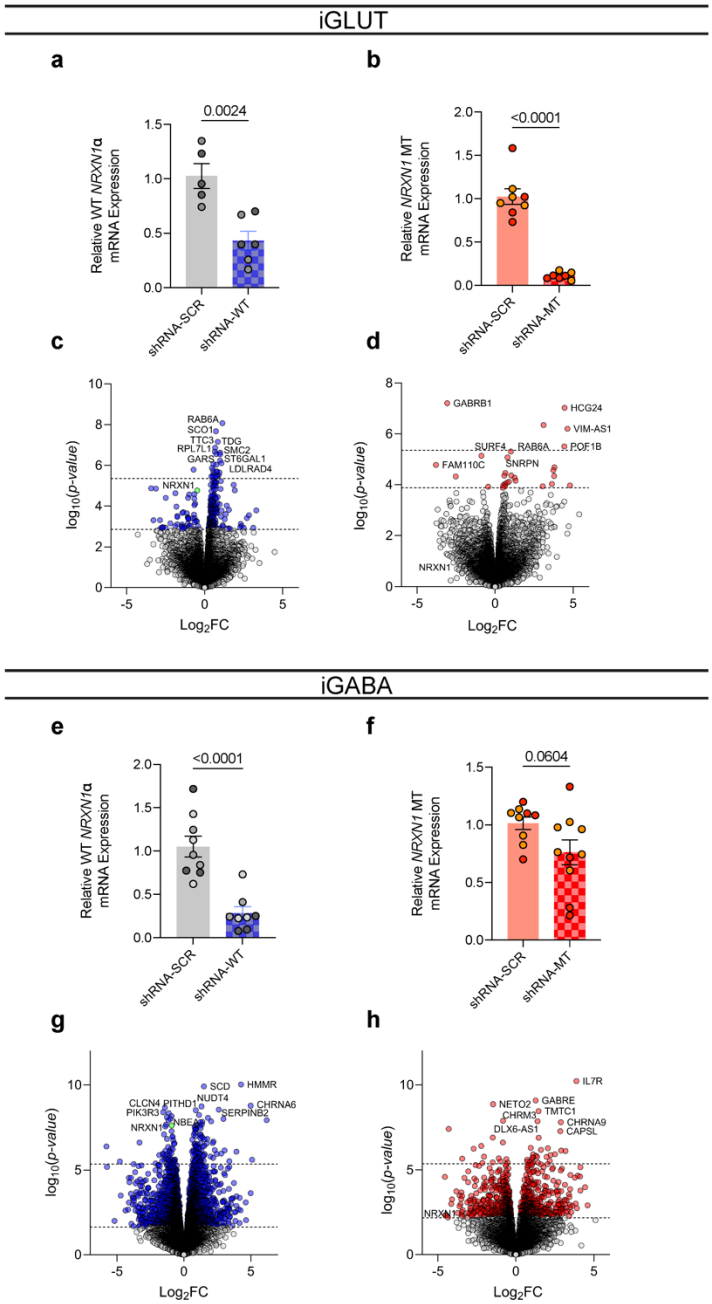

Extended Data Figure 6: *shRNA knockdown validation.* (a) Extent of shRNA knockdown on WT and (b) MT *NRXN1* expression in iGLUT neurons (n = 2 donors | 1-3 inductions). (c) Extent of

shRNA knockdown on WT and (d) MT *NRXN1* expression in iGABA neurons, (n = 2-3 donors | 1-3 inductions) Statistical tests used were Student's t-test.

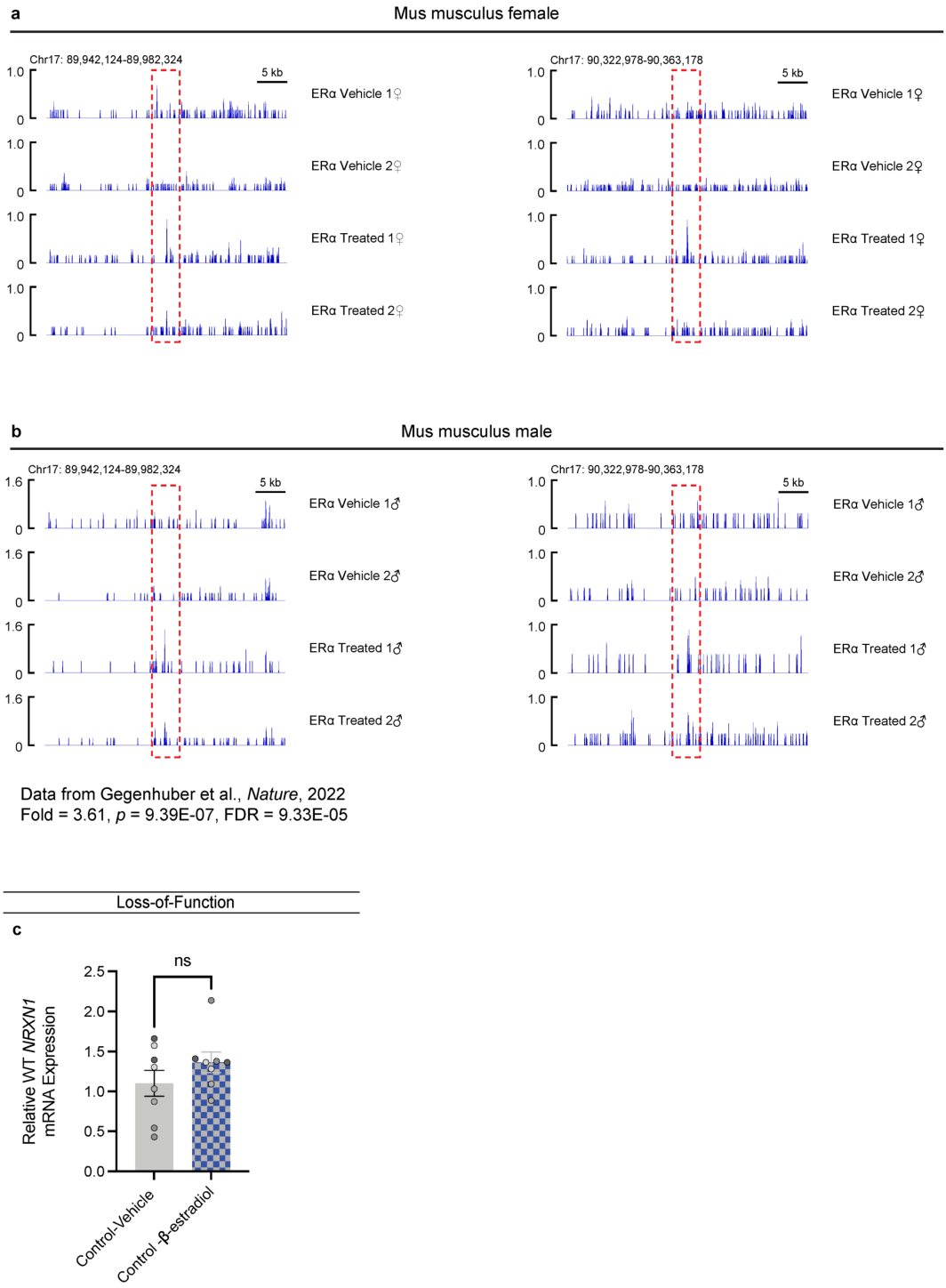

Extended Data Figure 7: *ChIP-seq enrichment of ER1 binding at NRXN1 loci in rodent brain.* (**a**) Female and (**b**) male mus musculus ChIP tracks of *NRXN1* locus, with red dashed areas

highlighting binding enrichment across vehicle and estradiol treated mice. (**c**) Effect of beta-estradiol on control donors (n = 16/4 | Representative).

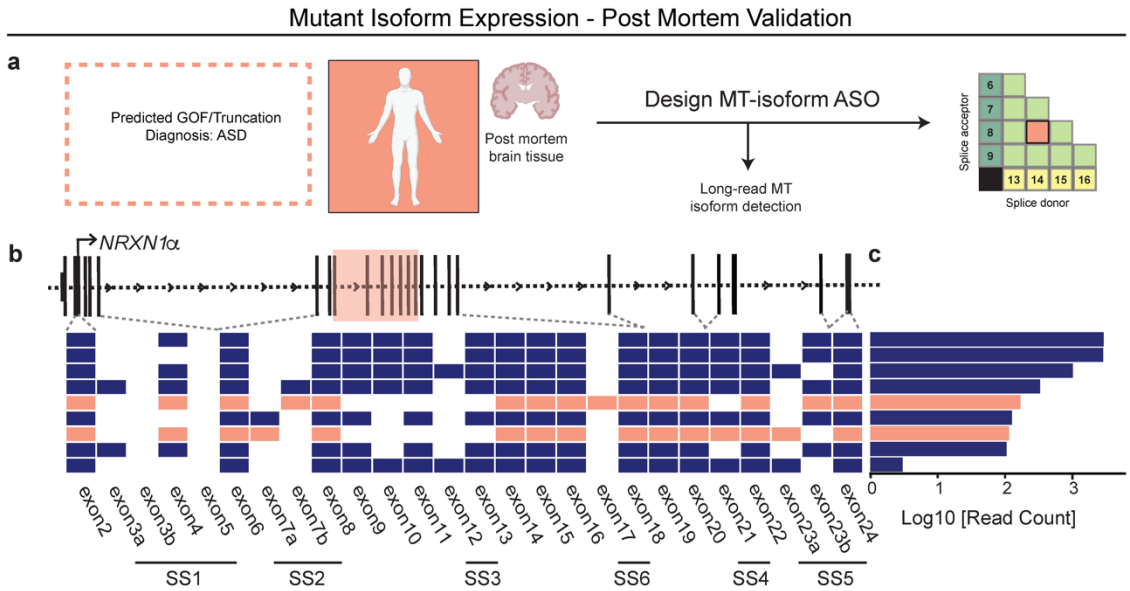

Extended Data Figure 8: *In-vivo validation of MT isoform expression from an unrelated autism NRXN1$^{+/-}$ patient.* (a) Schematic of novel NRXN1 autism patient, and GOF therapeutic targeting pipeline, with (b) schematic of the *NRXN1α* isoform structures, with each row representing a unique *NRXN1α* isoform and each column representing a *NRXN1* exon. The colored isoforms (navy, wildtype; peach, patient-specific) are spliced into the transcript while the blank exons are spliced out. (c) The abundance of each *NRXN1α* isoform by sample.

1047 **References**

1048 1. Sudhof, T. C. Synaptic Neurexin Complexes: A Molecular Code for the Logic of Neural
1049 Circuits. *Cell* **171**, 745–769 (2017).
1050 2. De Wit, J. & Ghosh, A. Specification of synaptic connectivity by cell surface interactions.
1051 *Nat. Rev. Neurosci.* **17**, 4–4 (2016).
1052 3. Gomez, A. M., Traunmüller, L. & Scheiffele, P. Neurexins: molecular codes for shaping
1053 neuronal synapses. *Nat. Rev. Neurosci.* **22**, 137–151 (2021).
1054 4. Schreiner, D. *et al.* Targeted Combinatorial Alternative Splicing Generates Brain Region-
1055 Specific Repertoires of Neurexins. *Neuron* **84**, 386–398 (2014).
1056 5. Fuccillo, M. V. *et al.* Single-Cell mRNA Profiling Reveals Cell-Type-Specific Expression of
1057 Neurexin Isoforms. *Neuron* **87**, 326–340 (2015).
1058 6. Marshall, C. R. *et al.* Contribution of copy number variants to schizophrenia from a genome-
1059 wide study of 41,321 subjects. *Nat Genet* **49**, 27–35 (2017).
1060 7. Matsunami, N. *et al.* Identification of Rare Recurrent Copy Number Variants in High-Risk
1061 Autism Families and Their Prevalence in a Large ASD Population. *PLoS ONE* **8**, e52239
1062 (2013).
1063 8. Moller, R. S. *et al.* Exon-disrupting deletions of NRXN1 in idiopathic generalized epilepsy.
1064 *Epilepsia* **54**, 256–64 (2013).
1065 9. Ching, M. S. L. *et al.* Deletions of *NRXN1* (neurexin-1) predispose to a wide spectrum of
1066 developmental disorders. *Am. J. Med. Genet. B Neuropsychiatr. Genet.* **153B**, 937–947
1067 (2010).
1068 10. Huang, A. Y. *et al.* Rare Copy Number Variants in NRXN1 and CNTN6 Increase Risk for
1069 Tourette Syndrome. *Neuron* **94**, 1101-1111 e7 (2017).

1070 11. Grayton, H. M., Missler, M., Collier, D. A. & Fernandes, C. Altered Social Behaviours in
1071 Neurexin 1α Knockout Mice Resemble Core Symptoms in Neurodevelopmental Disorders.
1072 *PLoS ONE* **8**, e67114 (2013).
1073 12. Pak, C. *et al.* Cross-platform validation of neurotransmitter release impairments in
1074 schizophrenia patient-derived *NRXN1* -mutant neurons. *Proc. Natl. Acad. Sci.* **118**,
1075 e2025598118 (2021).
1076 13. Pak, C. *et al.* Human Neuropsychiatric Disease Modeling using Conditional Deletion
1077 Reveals Synaptic Transmission Defects Caused by Heterozygous Mutations in NRXN1. *Cell*
1078 *Stem Cell* **17**, 316–328 (2015).
1079 14. Sebastian, R. *et al.* Schizophrenia-associated NRXN1 deletions induce developmental-
1080 timing- and cell-type-specific vulnerabilities in human brain organoids. *Nat. Commun.* **14**,
1081 3770 (2023).
1082 15. Flaherty, E. *et al.* Neuronal impact of patient-specific aberrant NRXN1alpha splicing. *Nat*
1083 *Genet* **51**, 1679–1690 (2019).
1084 16. Boxer, E. E. & Aoto, J. Neurexins and their ligands at inhibitory synapses. *Front. Synaptic*
1085 *Neurosci.* **14**, 1087238 (2022).
1086 17. Taoufik, E., Kouroupi, G., Zygogianni, O. & Matsas, R. Synaptic dysfunction in
1087 neurodegenerative and neurodevelopmental diseases: an overview of induced pluripotent
1088 stem-cell-based disease models. *Open Biol.* **8**, 180138 (2018).
1089 18. Ho, S.-M. *et al.* Rapid Ngn2-induction of excitatory neurons from hiPSC-derived neural
1090 progenitor cells. *Methods* **101**, 113–124 (2016).
1091 19. Zhang, Y. *et al.* Rapid single-step induction of functional neurons from human pluripotent
1092 stem cells. *Neuron* **78**, 785–98 (2013).
1093 20. Barretto, N. *et al.* ASCL1- and DLX2-induced GABAergic neurons from hiPSC-derived
1094 NPCs. *J Neurosci Methods* **334**, 108548 (2020).

1095 21. Yang, N. *et al.* Generation of pure GABAergic neurons by transcription factor programming.
1096 *Nat Methods* (2017) doi:10.1038/nmeth.4291.
1097 22. Li, Y. I. *et al.* Annotation-free quantification of RNA splicing using LeafCutter. *Nat Genet* **50**,
1098 151–158 (2018).
1099 23. Iijima, T. *et al.* SAM68 regulates neuronal activity-dependent alternative splicing of neurexin-
1100 1. *Cell* **147**, 1601–14 (2011).
1101 24. Iijima, T., Iijima, Y., Witte, H. & Scheiffele, P. Neuronal cell type-specific alternative splicing
1102 is regulated by the KH domain protein SLM1. *J Cell Biol* **204**, 331–42 (2014).
1103 25. Traunmuller, L., Gomez, A. M., Nguyen, T. M. & Scheiffele, P. Control of neuronal synapse
1104 specification by a highly dedicated alternative splicing program. *Science* **352**, 982–6 (2016).
1105 26. Traunmüller, L. *et al.* A cell-type-specific alternative splicing regulator shapes synapse
1106 properties in a trans-synaptic manner. *Cell Rep.* **42**, 112173 (2023).
1107 27. Ritchie, M. E. *et al.* limma powers differential expression analyses for RNA-sequencing and
1108 microarray studies. *Nucleic Acids Res.* **43**, e47–e47 (2015).
1109 28. Koopmans, F. *et al.* SynGO: An Evidence-Based, Expert-Curated Knowledge Base for the
1110 Synapse. *Neuron* **103**, 217-234.e4 (2019).
1111 29. Wu, T. *et al.* clusterProfiler 4.0: A universal enrichment tool for interpreting omics data. *The*
1112 *Innovation* **2**, 100141 (2021).
1113 30. Seah, C. *et al.* Modeling gene × environment interactions in PTSD using human neurons
1114 reveals diagnosis-specific glucocorticoid-induced gene expression. *Nat. Neurosci.* **25**,
1115 1434–1445 (2022).
1116 31. Lo Surdo, P. *et al.* SIGNOR 3.0, the SIGnaling network open resource 3.0: 2022 update.
1117 *Nucleic Acids Res.* **51**, D631–D637 (2023).
1118 32. Schafer, S. T. *et al.* Pathological priming causes developmental gene network
1119 heterochronicity in autistic subject-derived neurons. *Nat. Neurosci.* **22**, 243–255 (2019).

1120 33. Birey, F. *et al.* Assembly of functionally integrated human forebrain spheroids. *Nature* **545**,
1121 54–59 (2017).
1122 34. Yoon, S.-J. *et al.* Reliability of human cortical organoid generation. *Nat. Methods* **16**, 75–78
1123 (2019).
1124 35. Khan, T. A. *et al.* Neuronal defects in a human cellular model of 22q11.2 deletion syndrome.
1125 *Nat. Med.* **26**, 1888–1898 (2020).
1126 36. Zeng, L. *et al.* Functional Impacts of NRXN1 Knockdown on Neurodevelopment in Stem Cell
1127 Models. *PLoS ONE* **8**, e59685 (2013).
1128 37. Virtanen, M. A., Uvarov, P., Mavrovic, M., Poncer, J. C. & Kaila, K. The Multifaceted Roles
1129 of KCC2 in Cortical Development. *Trends Neurosci.* **44**, 378–392 (2021).
1130 38. Sohal, V. S. & Rubenstein, J. L. R. Excitation-inhibition balance as a framework for
1131 investigating mechanisms in neuropsychiatric disorders. *Mol. Psychiatry* **24**, 1248–1257
1132 (2019).
1133 39. Willsey, H. R. *et al.* Parallel in vivo analysis of large-effect autism genes implicates cortical
1134 neurogenesis and estrogen in risk and resilience. *Neuron* **109**, 1409 (2021).
1135 40. Gegenhuber, B., Wu, M. V., Bronstein, R. & Tollkuhn, J. Gene regulation by gonadal
1136 hormone receptors underlies brain sex differences. *Nature* **606**, 153–159 (2022).
1137 41. Roberts, T. C., Langer, R. & Wood, M. J. A. Advances in oligonucleotide drug delivery. *Nat.*
1138 *Rev. Drug Discov.* **19**, 673–694 (2020).
1139 42. Saito, Y. *et al.* Differential NOVA2-Mediated Splicing in Excitatory and Inhibitory Neurons
1140 Regulates Cortical Development and Cerebellar Function. *Neuron* **101**, 707-720.e5 (2019).
1141 43. Paz, I., Kosti, I., Ares, M., Cline, M. & Mandel-Gutfreund, Y. RBPmap: a web server for
1142 mapping binding sites of RNA-binding proteins. *Nucleic Acids Res.* **42**, W361–W367 (2014).
1143 44. Ghanbarian, H., Aghamiri, S., Eftekhary, M., Wagner, N. & Wagner, K.-D. Small Activating
1144 RNAs: Towards the Development of New Therapeutic Agents and Clinical Treatments. *Cells*
1145 **10**, 591 (2021).

1146 45. Subramanian, A. *et al.* A Next Generation Connectivity Map: L1000 Platform and the First
1147 1,000,000 Profiles. *Cell* **171**, 1437-1452.e17 (2017).
1148 46. Yilmaz, C. *et al.* Neurosteroids as regulators of neuroinflammation. *Front. Neuroendocrinol.*
1149 **55**, 100788 (2019).
1150 47. Brunet De Courssou, J.-B., Durr, A., Adams, D., Corvol, J.-C. & Mariani, L.-L. Antisense
1151 therapies in neurological diseases. *Brain* **145**, 816–831 (2022).
1152 48. Ingusci, S., Verlengia, G., Soukupova, M., Zucchini, S. & Simonato, M. Gene Therapy Tools
1153 for Brain Diseases. *Front. Pharmacol.* **10**, 724 (2019).
1154 49. Lin, H.-C. *et al.* NGN2 induces diverse neuron types from human pluripotency. *Stem Cell*
1155 *Rep.* **16**, 2118–2127 (2021).
1156 50. Zafra, F. & Piniella, D. Proximity labeling methods for proteomic analysis of membrane
1157 proteins. *J. Proteomics* **264**, 104620 (2022).
1158 51. Bell, J. Stratified medicines: towards better treatment for disease. *The Lancet* **383**, S3–S5
1159 (2014).
1160 52. Tsimberidou, A. M. *et al.* Molecular tumour boards — current and future considerations for
1161 precision oncology. *Nat. Rev. Clin. Oncol.* **20**, 843–863 (2023).
1162 53. Zhang, H., Colclough, K., Gloyn, A. L. & Pollin, T. I. Monogenic diabetes: a gateway to
1163 precision medicine in diabetes. *J. Clin. Invest.* **131**, e142244 (2021).
1164 54. Sullivan, P. F. & Geschwind, D. H. Defining the Genetic, Genomic, Cellular, and Diagnostic
1165 Architectures of Psychiatric Disorders. *Cell* **177**, 162–183 (2019).
1166 55. Gerasimavicius, L., Livesey, B. J. & Marsh, J. A. Loss-of-function, gain-of-function and
1167 dominant-negative mutations have profoundly different effects on protein structure. *Nat.*
1168 *Commun.* **13**, 3895 (2022).
1169 56. Wang, L. *et al.* Analyses of the autism-associated neuroligin-3 R451C mutation in human
1170 neurons reveal a gain-of-function synaptic mechanism. *Mol. Psychiatry* **29**, 1620–1635
1171 (2024).

1172 57. Pinggera, A. *et al.* New gain-of-function mutation shows CACNA1D as recurrently mutated
1173 gene in autism spectrum disorders and epilepsy. *Hum. Mol. Genet.* **26**, 2923–2932 (2017).
1174 58. Clark, M. B. *et al.* Long-read sequencing reveals the complex splicing profile of the
1175 psychiatric risk gene CACNA1C in human brain. *Mol. Psychiatry* **25**, 37–47 (2020).
1176 59. Brunklaus, A. *et al.* Gene variant effects across sodium channelopathies predict function
1177 and guide precision therapy. *Brain* **145**, 4275–4286 (2022).
1178 60. Sanders, S. J. *et al.* Progress in Understanding and Treating SCN2A-Mediated Disorders.
1179 *Trends Neurosci.* **41**, 442–456 (2018).
1180 61. Kim, G., Gautier, O., Tassoni-Tsuchida, E., Ma, X. R. & Gitler, A. D. ALS Genetics: Gains,
1181 Losses, and Implications for Future Therapies. *Neuron* **108**, 822–842 (2020).
1182 62. Balendra, R. & Isaacs, A. M. C9orf72-mediated ALS and FTD: multiple pathways to disease.
1183 *Nat. Rev. Neurol.* **14**, 544–558 (2018).
1184 63. Prakasam, R. *et al.* LSD1/PRMT6-targeting gene therapy to attenuate androgen receptor
1185 toxic gain-of-function ameliorates spinobulbar muscular atrophy phenotypes in flies and
1186 mice. *Nat. Commun.* **14**, 603 (2023).
1187 64. Chintalaphani, S. R., Pineda, S. S., Deveson, I. W. & Kumar, K. R. An update on the
1188 neurological short tandem repeat expansion disorders and the emergence of long-read
1189 sequencing diagnostics. *Acta Neuropathol. Commun.* **9**, 98 (2021).
1190 65. Rhee, H. J. *et al.* An Autaptic Culture System for Standardized Analyses of iPSC-Derived
1191 Human Neurons. *Cell Rep.* **27**, 2212-2228.e7 (2019).
1192 66. Sloan, S. A., Andersen, J., Pașca, A. M., Birey, F. & Pașca, S. P. Generation and assembly
1193 of human brain region–specific three-dimensional cultures. *Nat. Protoc.* **13**, 2062–2085
1194 (2018).
1195 67. Dobin, A. *et al.* STAR: ultrafast universal RNA-seq aligner. *Bioinformatics* **29**, 15–21 (2013).
1196 68. Liao, Y., Smyth, G. K. & Shi, W. featureCounts: an efficient general purpose program for
1197 assigning sequence reads to genomic features. *Bioinformatics* **30**, 923–930 (2014).

1198 69. Robinson, M. D., McCarthy, D. J. & Smyth, G. K. edgeR : a Bioconductor package for
1199 differential expression analysis of digital gene expression data. *Bioinformatics* **26**, 139–140
1200 (2010).
1201 70. Hoffman, G. E. *et al.* Transcriptional signatures of schizophrenia in hiPSC-derived NPCs
1202 and neurons are concordant with post-mortem adult brains. *Nat. Commun.* **8**, 2225 (2017).
1203 71. Newman, A. M. *et al.* Determining cell type abundance and expression from bulk tissues
1204 with digital cytometry. *Nat. Biotechnol.* **37**, 773–782 (2019).
1205 72. Hoffman, G. E. & Schadt, E. E. variancePartition: interpreting drivers of variation in complex
1206 gene expression studies. *BMC Bioinformatics* **17**, 483 (2016).
1207 73. Bray, N. L., Pimentel, H., Melsted, P. & Pachter, L. Near-optimal probabilistic RNA-seq
1208 quantification. *Nat. Biotechnol.* **34**, 525–527 (2016).
1209 74. De Marinis, I., Lo Surdo, P., Cesareni, G. & Perfetto, L. SIGNORApp: a Cytoscape 3
1210 application to access SIGNOR data. *Bioinformatics* **38**, 1764–1766 (2022).
1211 75. Stuart, T. *et al.* Comprehensive Integration of Single-Cell Data. *Cell* **177**, 1888-1902.e21
1212 (2019).
1213 76. Urresti, J. *et al.* Cortical organoids model early brain development disrupted by 16p11.2
1214 copy number variants in autism. *Mol. Psychiatry* **26**, 7560–7580 (2021).
1215 77. Yang, X. *et al.* Identification and validation of genes affecting aortic lesions in mice. *J. Clin.*
1216 *Invest.* **120**, 2414–2422 (2010).
1217 78. Kurtenbach, S. & William Harbour, J. SparK: A Publication-quality NGS Visualization Tool.
1218 Preprint at https://doi.org/10.1101/845529 (2019).
1219